The Journal of Chemical Physics ARTICLE scitation.org/journal/jcp

Effects of pore size on water dynamics in mesoporous silica

Cite as: J. Chem. Phys. 152, 154704 (2020); doi: 10.1063/1.5145326
Submitted: 16 January 2020 • Accepted: 24 March 2020 •
Published Online: 17 April 2020

Steven A. Yamada,[1] Samantha T. Hung,[1] Ward H. Thompson,[2,a)] and Michael D. Fayer[1,b)]

AFFILIATIONS

[1] Department of Chemistry, Stanford University, Stanford, California 94305, USA
[2] Department of Chemistry, University of Kansas, Lawrence, Kansas 66045, USA

[a)] **Email:** wthompson@ku.edu. **Tel.:** (785) 864-3980
[b)] **Author to whom correspondence should be addressed:** fayer@stanford.edu. **Tel.:** (650) 723-4446

ABSTRACT

Water confined in mesoporous silica plays a central role in its many uses ranging from gas sorption to nanoconfined chemical reactions. Here, the influence of pore diameter (2.5–5.4 nm) on water hydrogen bond (H-bond) dynamics in MCM41 and SBA15 mesoporous silicas is investigated using femtosecond infrared vibrational spectroscopy and molecular dynamics simulations on selenocyanate ($SeCN^-$) anions dissolved in the pores. As shown recently, $SeCN^-$ spectral diffusion is a reliable probe of surrounding water H-bond structural motions. Additionally, the long CN stretch vibrational lifetime facilitates measurement of the full range of confined dynamics, which are much slower than in bulk water. The simulations shed light on quantitative details that are inaccessible from the spatially averaged observables. The dependence of $SeCN^-$ orientational relaxation and that of spectral diffusion on the distance from the silica interface are quantitatively described with an exponential decay and a smoothed step-function, respectively. The distance-dependence of both quantities is found to be independent of the diameter of the pores, and the spatial distribution of $SeCN^-$ is markedly non-uniform, reaching a maximum between the interface and the pore center. The results indicate that the commonly invoked two-state, or core–shell, model is a more appropriate description of spectral diffusion. Using these insights, we model the full time-dependence of the measured dynamics for all pore sizes and extract the "core" and "shell" dynamical correlation functions and $SeCN^-$ spatial probability distributions. The results are critically compared to those for water confined in reverse micelles.

I. INTRODUCTION

Water confined in mesoporous silica has diverse applications including adsorption of metal ions[1] and volatile organic molecules[2] from wastewater and air, CO_2 capture from humidified flue gases,[3] the folding of encapsulated proteins,[4,5] and nanoconfined reactions in aqueous solution.[6] Despite enduring interest in these systems, predicting how the properties of water scale with the size of the nanostructures remains a significant challenge. Typically, changes in the structure and dynamics of liquids from their bulk values are observed when the separation from an interface becomes less than ~10 molecular diameters.[7–18] Exceptions have been reported, as in the case of ionic liquids (ILs), where interfacial effects on the dynamics are observed over tens to hundreds of nanometers (constituting hundreds to thousands of molecules) in porous membranes[19] and thin films.[20,21] In the case of water, which has a single layer statistical thickness of ~2.5 Å,[22,23] differences from the bulk liquid appear once the distances from an interface approach a few nanometers.[9–16,18,23–31] These results imply that the influence of the interface decays rapidly, i.e., on characteristic length scales of a few water diameters.

Although confinement generally slows liquid dynamics, even in situations of extreme confinement such as water "nanopools" in reverse micelles (RMs)[13,15] and mesoporous silica,[18] femtosecond to picosecond hydrogen bond (H-bond) network fluctuations are observed. Measuring the evolution of these fast time scales with spatial resolution on molecular length scales inside a nanoconfining system poses a significant challenge as the required femtosecond and sub-nanometer resolution is beyond available methods.[17] In general, the distance-dependence of the dynamics and the spatial probability distribution of the molecular species in the nanostructure are necessary to model the measured dynamics.[17] For the

description to be reliable, measurements on a series of confining framework sizes are needed to rigorously test the validity of the proposed models.[7,14,16,17,21,32]

In the commonly applied two-state, or core–shell, model, the dynamics assume distinct values in the "core" and "shell" regions of the nanostructure and transition between them as a step function.[17,33] For a cylindrical pore of radius R and shell thickness Δ, the dynamics as a function of distance from the center of the pore, ρ, can be expressed as

$$P(t;\rho) = P_{\text{core}}(t) + (P_{\text{shell}}(t) - P_{\text{core}}(t))\theta[\rho - (R - \Delta)], \quad (1)$$

where $P_{\text{core}}(t)$ and $P_{\text{shell}}(t)$ are the dynamics in the core and shell regions and $\theta(x)$ is the Heaviside step function. The two-state model was used to describe the dielectric relaxation time distributions attributed to interfacial and bulk-like H-bond forming diols confined in sol–gel glasses[7] and in a 2D IR study to predict the amplitudes of spectral diffusion components sensed by a silane probe tethered to the surface of spherical silica mesopores.[32] In contrast, an exponentially decaying distance-dependence was assumed to model the fast spectral diffusion of anionic probes in RMs of changing diameter[14] and at a single time delay for a series of IL thin films of varying thicknesses.[21] In the RM study, the characteristic length of the exponential was assumed to vary with radius based on simulation results which found this to apply to the rotational dynamics of water.[13] In all studies employing free probe molecules, the probes were assumed to be uniformly distributed in nanostructures.[7,14,21] The complete time-dependence of the correlation functions in the 2D IR studies was not modeled because the lifetimes of the probes limited the observations to the fast dynamics and additional assumptions would need to be included.[14,21,32] For example, it is unclear whether different time scales follow different characteristic lengths and whether the interfacial dynamics and lengths depend on the size of the nanostructure.

In addition to its many applications involving confined water, mesoporous silica is a useful system for understanding the influence of confinement on ultrafast water dynamics because of the availability of a range of highly uniform pore diameters.[34–36] To address the influence of pore size on water dynamics, we studied pores in the diameter range of 2.5–5.4 nm with polarized IR pump–probe experiments, 2D IR spectroscopy, and molecular dynamics (MD) simulations. The reorientation and spectral diffusion of selenocyanate ($SeCN^-$) dissolved in the water is used to probe the H-bond structural dynamics. H-bond dynamics, which couple to the frequency of the vibrational mode, lead to a time-dependent decorrelation between the initially excited and final frequencies detected, i.e., spectral diffusion. SCN^- and $SeCN^-$ vibrational probes have been used to investigate intermolecular vibrational energy transfer in ion/water H-bond complexes,[37] contact ion pair dissociation times,[38,39] and the role of cation identity, surface interactions, and confinement on dynamic observables in aqueous systems.[18,40–42] Recently, an analysis of $SeCN^-$ CN stretch dynamics in bulk D_2O demonstrated that the spectral diffusion time scales agree with those observed when the water OH stretching mode is directly probed.[43] Additionally, the long CN stretch vibrational lifetime of $SeCN^-$ (~36 ps), in contrast to that of the HOD hydroxyl stretch (~0.7 ps), provides a large experimental time window over which the dynamics can be observed. The rotation of $SeCN^-$, although qualitatively different from that of water,[43] is constrained by the surrounding H-bond structure, providing further details on the nature of the interactions under nanoscale confinement.

The analysis of the simulations and nonlinear spectroscopic observables shows that the concept of core and shell regions with homogeneous dynamics does not apply to the rotational dynamics, which accelerate exponentially with an increase in the distance from the silica surface. The characteristic length of the decay is ~2 Å or about the size of a water molecule.[22] Water rotational dynamics in RMs were also found to exhibit an exponential spatial dependence in a previous simulation study.[13] The experiments and simulations on water in the SiO_2 pores show that the orientational relaxation of $SeCN^-$ at the distance of closest approach, d_0 = 3 Å, occurs on a 14 ± 1 ps time scale, which is close to the 13 ps reorientation time constant of $SeCN^-$ near the surface of "large" RMs.[16] This result suggests that the chemical natures of the silica and surfactant interfaces have a similar (or perhaps minor) influence on the dynamics, an idea proposed in studies that observed the same water dynamics within experimental error at the interface of charged (AOT) and neutral (Igepal) RMs.[12] In contrast, the spectral diffusion is better described by a two-state model, although the step transition between the shell and the core is not sharp. The width of the transition region is similar to the thickness of a single water layer. This analysis differs from studies that have assumed an exponential form for the acceleration of the vibrational dynamics with the distance from the interface of RMs and IL thin films.[14,21] The spectral diffusion at the interface of the silica pores consists of 1.9 ps and 14.6 ps components. Contrasting these time scales with the core (and bulk liquid) values of 0.5 ps and 1.6 ps indicates dramatically slower H-bond dynamics near the surface. Finally, in contrast to the usual assumption of a uniformly distributed probe in the nanostructure,[7,14,21] the simulations and their consistency with the experiments indicate that the $SeCN^-$ distributions are peaked somewhere between the surface and the center of the pore, and the location of this maximum depends on the pore radius.

II. EXPERIMENTAL PROCEDURES

A. Sample characterization and preparation

The experiments focus on five samples: bulk 0.3M KSeCN in D_2O and this same solution confined in roughly cylindrical silica mesopores of diameters of 2.5 ± 0.2 nm, 2.8 ± 0.1 nm, 4.2 ± 0.5 nm, and 5.4 ± 0.5 nm. The two smallest pores are MCM41 and the larger two are SBA15. The 2.8 nm sample was purchased from ACS Material, while the remaining samples were purchased from Sigma-Aldrich. The bulk[43] and 2.5 nm[18] systems were discussed in detail previously. The analysis of the bulk system showed that the linear IR spectrum and dynamical observables were invariant over a concentration range from 0.1 M to 0.5 M, demonstrating that the concentrations are within the dilute limit.[43,60] Previous work has shown that KSCN concentrations of several molar are required to observe the onset of ion pairing, changes in viscosity, and the slowing of dynamic observables.[40,41] In the study of the 2.5 nm pore, no effects of ion pairing, such as a blue-shifted shoulder in the linear IR spectrum,[38,39] were observed, indicating that the concentration of 0.3 M is also within the dilute limit under nanoconfinement in silica.[18] These observations justify the lower concentration of $SeCN^-$

used in the earlier MD simulations[18,43] and in the present work (*vide infra*). The surface areas, pore size distributions (Fig. S1 of the supplementary material), and primary mesopore volumes of the materials were determined at the Soft & Hybrid Materials Facility (SMF) at the Stanford Nano Shared Facilities (SNSF), as previously described.[18] These quantities are tabulated in Table I. A sedimentation procedure was used to reduce the particle size of the samples to eliminate the larger particles, which generated significant scattered light in the experiments.[18] The dried powders were mixed in the KSeCN/D_2O solution and then filtered to remove excess solution. To ensure complete hydration of the pores, the samples were equilibrated overnight in a home-built hydration chamber by flowing water saturated [~100% relative humidity (RH)] N_2 (g) vapor over the particles.[18]

B. Infrared spectroscopy

The linear and nonlinear spectroscopic techniques in this work have been described in detail previously;[18,43] brief descriptions of the nonlinear techniques, 2D IR spectroscopy, and polarization selective pump–probe (PSPP) experiments are provided here.

The 2D IR pulse sequence consists of four pulses. The first two pulses in the sequence, pump pulses 1 and 2, label and store the initial vibrational frequencies, ω_1, of the ensemble of CN stretches of the vibrational probe, $SeCN^-$. A Fourier transform over the time delay, τ, between the two pump pulses forms the initial frequency axis of the 2D spectrum, ω_1. The time delay, T_w, between pulse 2 and pulse 3 (also known as the probe pulse) is the waiting time. During this period, the structure of the water hydrogen bond network fluctuates and reorganizes around the probe molecules, causing their vibrational frequencies to change. These three input pulses generate a nonlinear polarization in the sample, which leads to the emission of the fourth pulse, or vibrational echo signal. The echo pulse is collinear with the probe pulse, which acts as the local oscillator (LO) to heterodyne detect the echo signal. The signal/LO beam is directed into a monochromator, which acts as a spectrograph, and the frequency dispersed signal/LO beam is detected with an IR array detector. As τ is scanned, an interferogram is recorded at each frequency (pixel of the array detector). Numerical Fourier transformation of these interferograms gives the ω_1 (initial frequency) axis of the 2D IR spectrum. The spectrograph generates an experimental Fourier transform, which gives the final frequency axis of the 2D spectrum, ω_3.

Qualitatively, the experiment works as follows: Pulse 1 labels the frequencies of the probes across the inhomogeneously broadened absorption spectrum. Pulse 2, a short time later, stores the information. The system, in this case water in the mesopores, is allowed to structurally evolve for the waiting time, T_w. Then, pulse 3 initiates a readout, and the echo pulse reports on the probe frequencies after the evolution time T_w. During T_w, the water structure evolves, causing the local environments of the vibrational probes to change, which in turn changes the probe frequencies. 2D spectra are recorded as a function of T_w. As T_w increases, the shape of the 2D spectrum changes because the final frequencies differ more and more from the initial frequencies. At short times, the band shape is elongated along the diagonal line of the 2D spectrum (the line $\omega_3 = \omega_1$), owing to the high correlation between the initial (ω_1) and final (ω_3) frequencies. At later times, spectral diffusion dynamics have diminished the correlation between ω_1 and ω_3 frequencies, resulting in an increasingly round 2D band shape. The frequencies change because the structure changes. Therefore, the T_w dependent changes in frequencies are measured to report on the structural evolution of water.

The time scales of the spectral diffusion occurring over the T_w period can be extracted from quantitative analysis of the time-dependent 2D band shape.[44–46] The T_w dependent 2D IR data are evaluated to obtain the frequency–frequency correlation function (FFCF), which is the connection between the experimental observables and the molecular level dynamics. To quantify the T_w dependence of the 2D IR spectra to yield the spectral diffusion dynamics, the center line slope (CLS) method was used.[44,45] It has been shown that the CLS(T_w) decay is the normalized frequency–frequency correlation function (FFCF), which is the probability that the vibrational probe with a frequency at time $t = 0$ has the same frequency at a later time, averaged over all the frequencies in the inhomogeneously broadened absorption line shape.[44,45] The complete FFCF is typically modeled with the Kubo ansatz,[46,47]

$$\mathrm{FFCF} = C_\omega(t)\langle\delta\omega(0)^2\rangle = \langle\delta\omega(t)\delta\omega(0)\rangle = \sum_i \Delta_i^2 \exp[-t/\tau_i], \quad (2)$$

where $C_\omega(t)$ is the normalized FFCF and the frequency fluctuation, $\delta\omega(t) = \omega(t) - \langle\omega\rangle$, is the difference between the instantaneous frequency at time t and the average frequency, $\omega(t)$ and $\langle\omega\rangle$, respectively, while Δ_i and τ_i are the amplitude of the frequency fluctuation and time constant of the ith decay pathway, respectively. From the CLS(T_w) and the IR absorption spectrum, the full FFCF can be determined.

PSPP spectroscopy is a transient absorption experiment.[46,48,49] A single pump pulse excites the sample. After a time delay, t, the probe pulse interacts with the sample. The PSPP signal is the transient intensity difference in the probe with and without the pump pulse. The experiment is performed in "parallel" and "perpendicular" polarization configurations. In both configurations, the pump and probe are linearly polarized at 45° and 0° (in the plane of the optical table), respectively. After the sample, a polarizer in a computer-controlled rotation mount resolves the probe pulse (the signal) at +45° or −45°, which correspond to the parallel, $S_\parallel(t)$, and perpendicular, $S_\perp(t)$, signals, respectively. The vibrational population relaxation and rotational dynamics can be extracted from these two signals via the expressions[48,49]

$$P(t) = \left[S_\parallel(t) + 2S_\perp(t)\right]/3, \quad (3)$$

$$r(t) = \frac{S_\parallel(t) - S_\perp(t)}{S_\parallel(t) + 2S_\perp(t)} = 0.4C_2(t), \quad (4)$$

TABLE I. Sample properties. S_{BET}: Specific BET surface area, D: Pore diameter, V_p: Primary mesopore volume, and V_t: Total pore volume.

Sample	S_{BET} (m^2/g)	D (nm)	V_p (cm^3/g)	V_t (cm^3/g)
MCM41	960 ± 30	2.5 ± 0.2	0.71 ± 0.03	0.91 ± 0.07
MCM41	950 ± 70	2.8 ± 0.1	0.75 ± 0.06	0.82 ± 0.05
SBA15	560 ± 80	4.2 ± 0.5	0.48 ± 0.06	0.62 ± 0.06
SBA15	840 ± 100	5.4 ± 0.5	0.8 ± 0.1	1.1 ± 0.2

where $P(t)$ is the isotropic pump–probe signal decay (vibrational lifetime) and $r(t)$ is the orientational anisotropy. $C_2(t)$ is the second Legendre polynomial orientational relaxation correlation function. $P(t)$ is shown as a function of pore size in Fig. S2 of the supplementary material. The vibrational lifetimes of $SeCN^-$ are plotted as a function of the reciprocal pore radius in Fig. S3 of the supplementary material. The lifetimes gradually decrease from the bulk value (~36 ps) as the pore becomes smaller, although the variation is small relative to the experimental error. Nonetheless, the trend is suggestive and consistent with lifetime calculations as a function of increasing confinement.[50]

The mesoporous silica samples studied here are in the form of powders composed of many particles. When the pump pulses used in 2D IR and PSPP spectroscopy interact with the particles, a significant portion of the light will scatter into the signal direction, leading to the contamination of the desired third order signals by scattered light.[51,52] These scatter signals must be eliminated to cleanly extract the 2D IR and PSPP data of interest. The specific polarization and phase cycling methods used to cleanly collect the signals in this work have been discussed in considerable detail in a previous publication.[18]

III. SIMULATION DETAILS

The dynamical and spectroscopic properties of $SeCN^-$ in bulk and confined D_2O have also been modeled using MD simulations. Many of the details have been given previously,[18,43] and here, we only briefly summarize the approach. The $SeCN^-$ solute is described as a rigid, linear molecule with fixed charges in a symmetric distribution ($q_{Se} = q_N = -0.55$, $q_C = 0.1$); the full force field description has been given in a prior publication.[43] The D_2O molecules are described by the SPC/E model[53] and held rigid using the SHAKE algorithm.[54]

Model amorphous silica pores of approximate diameter 2.4 nm and 4.4 nm were generated using an approach developed previously.[55,56] Briefly, the pore is formed by heating crystalline silica to 8000 K, growing a Lennard-Jones cylinder "resist" in the center of the silica, and cooling it back to room temperature to form an unfunctionalized pore. The interior of the pore is then terminated with –OH groups by adding water across the longer Si–O bonds (OH is bound to Si and H is bound to O). In the MD simulations, the pore framework is held fixed, while the silanols are allowed to move according to potentials given in an early publication.[18] The interactions with the water and $SeCN^-$ are those of Gulmen and Thompson,[56] except that ClayFF charges are used[57] based on comparisons between simulations and experiments in 2.4 nm diameter pores.[18]

The 4.4 nm pore was filled with water from MD simulations of the pore in contact with a water reservoir at constant pressure; this is expected to give equivalent results to the grand canonical Monte Carlo simulations used to fill the 2.4 nm pore. After filling with water, one molecule is substituted for an $SeCN^-$ solute with the result that the larger pore contains 3009 D_2O and 1 $SeCN^-$ with 190 SiOH and 37 $Si(OH)_2$ groups on the surface giving ~3.2 OH/nm^2.

The details of the smaller (2.4 nm) pore MD simulations have been presented.[18] For the larger pore, five independent trajectories were propagated with a time step of 1 fs and configurations written every 12 fs. The trajectories differed in the initial velocities and included a 2 ns equilibration period before an 18 ns data collection stage. Both Lennard-Jones and electrostatic interactions were calculated with a cutoff radius of 12 Å, and the damped-shifted force method[58] with a damping parameter of 0.2 was used to describe the long-range electrostatics. Errors in calculated quantities are 95% confidence intervals from block averaging (with each of the five trajectories as a block) based on the Student's t-distribution.[59]

The vibrational spectroscopy of the CN stretch of $SeCN^-$ is evaluated using an empirical map that was previously developed based on density functional theory calculations of $SeCN^-$ in bulk D_2O. The map has been described in detail.[43] Briefly, it represents the CN stretching frequencies as a linear function of the field exerted on the C atom in the direction along the CN bond. The field is calculated from the SPC/E charges of the water and the ClayFF charges of the pore for all water molecules, single silanol or geminal groups, and silica atoms within 10 Å of the $SeCN^-$ center-of-mass.

IV. RESULTS AND DISCUSSION

A. Experiments

1. Linear IR spectra

The linear absorption spectra of $SeCN^-$ in bulk and confined D_2O are presented in Fig. 1. In agreement with previous results for the smallest pore (2.5 nm),[18] the band centers and full width at half-maxima (FWHM) are indistinguishable from the bulk liquid values of 2075 cm^{-1} and 33 cm^{-1}, respectively (Table II). However, the bulk spectrum has a long tail on the red side of the line that is absent in the pore spectra. The long tail has been attributed to a non-Condon effect that causes the transition dipoles on the red side of the line to be larger.[43,60] For $SeCN^-$, the stronger axial hydrogen bonds cause a blueshift, while the more numerous but weaker equatorial H-bonds produce a redshift. The redshift is associated with an overall stronger transition dipole.[43] The absence of the tail in the pores suggests that the population of very weak $SeCN^-$/water H-bonds is reduced in the pores.

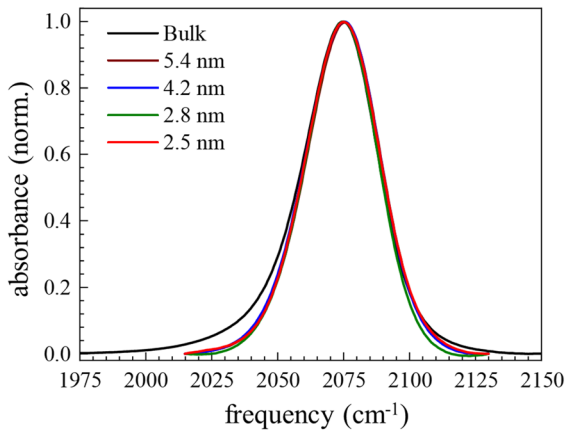

FIG. 1. Linear-IR spectra of the $SeCN^-$ CN stretch in bulk D_2O (black curve) and in D_2O confined in silica pores of sizes 5.4 nm (brown curve), 4.2 nm (blue curve), 2.8 nm (green curve), and 2.5 nm (red curve). The spectra are more symmetric under confinement; however, the center and FWHM are unchanged from the bulk values.

TABLE II. Line shape and distribution parameters. Centers and FWHM for the experimental (expt.) and simulated (sim.) FT IR spectra, $I(\omega)$, frequency distributions, $P(\omega)$, and spectral densities, $P_\mu(\omega)$, for $SeCN^-$ in bulk D_2O and nanoconfined D_2O in silica pores of different sizes. The parameters for the bulk liquid and for the smallest pore size are reproduced with permission from Yamada *et al.*, J. Chem. Phys. **146**, 234501 (2017). Copyright 2017 AIP Publishing LLC and Yamada *et al.*, J. Phys. Chem. C **123**, 5790–5803 (2019). Copyright 2019 American Chemical Society, respectively.

	Line shape/distribution	Sample	Center (cm^{-1})	FWHM (cm^{-1})
Expt.	$I(\omega)$	Bulk	2074.7 ± 0.1	32.9 ± 0.1
		5.4 nm	2075.5 ± 0.9	32 ± 1
		4.2 nm	2075.2 ± 0.5	33 ± 1
		2.8 nm	2074.8 ± 0.4	31.5 ± 0.1
		2.5 nm	2075.1 ± 0.7	32.6 ± 0.7
Sim.	$I(\omega)$	Bulk	2075	38.5
		4.4 nm	2075	41
		2.4 nm	2074	61
	$P(\omega)$	Bulk	2077	59.6
		4.4 nm	2076	60
		2.4 nm	2077	78
	$P_\mu(\omega)$	Bulk	2072	58.8
		4.4 nm	2073	60
		2.4 nm	2071	77

The invariance of the center frequency and the FWHM is notable considering the systematic redshift of the same band in AOT RMs of decreasing diameter in the range ~8.4 nm to ~2.6 nm.[16] As the diameter of the RMs was decreased further to ~1.7 nm and ~1.4 nm, a more dramatic redshift from the bulk center position was observed. However, the nature of the confinement in the RM system differs in several ways from that in mesoporous silica. In RMs, the water pools are roughly spherical,[13,26] whereas in silica, the water is confined to a cylindrical pore.[18] This difference in geometry means that in RMs, the influence of the interface acts from all directions (3D), while in the silica pores, the interface acts only in the two directions normal to the long axis of the pore (2D). This additional dimension of confinement also affects the long-range electrostatic effects of the confined water. Thus, the confinement is more extreme in RMs relative to cylindrical silica pores of comparable diameter. In contrast to the soft interface of RMs, which is composed of negatively charged surfactant molecules,[13,26] the hard surface of the silica pores consists of heterogeneously distributed hydrophilic silanol dense and silanol free regions.[61–64] These differences in the geometry, chemistry, dynamics, and charge of the RM interface may lead to the redshift in the $SeCN^-$ band that is not seen in comparably sized silica pores.

Similar to the $SeCN^-$ spectra, the IR spectrum of the OH stretch of dilute HOD in D_2O showed very little change upon increasing confinement in controlled-pore glasses down to 1 nm in diameter.[25] This was explained by simulations that showed that the main change in the OH stretch frequency is associated with OH groups donating an H-bond to the silica pore oxygens.[30] These are poorer H-bond acceptors than water, which leads to a blueshift. However, these blue-shifted OH groups are not observed in the IR spectrum because of their weaker transition dipole moments; they are observed in both measured and simulated Raman spectra[30,65] because the transition polarizability (unlike the dipole) does not change significantly with H-bond strength. More dramatic changes in the absorption spectrum of the OD stretch of dilute HOD in H_2O were observed upon confinement in nanostructured materials such as RMs or Nafion fuel-cell membranes.[9,11,66,67] A pronounced blueshift and non-monotonic variation in the FWHM were observed as the RM size decreased.[13] In Nafion, the OD stretch spectrum also blue-shifted and broadened relative to bulk water.[66,67] A blueshift in this band indicates that the H-bond interactions are weakened and/or reduced relative to those in bulk water.[68] Another difference between these spectra and the spectra in Fig. 1 is that they could be linearly decomposed into distinct "core" and "shell" spectra.[11,15,66,67] The "core" spectrum was represented by the bulk spectrum, while the "shell" spectrum was taken to be the spectrum for the smallest RM or minimum hydration spectrum in Nafion. This type of spectral decomposition also worked well for the $SeCN^-$ band in RMs.[16] The weak size-dependence of the linear spectra in Fig. 1 suggests that the H-bond interactions in mesoporous silica are different from these other systems. It is also possible that the pore size must be further decreased to observe significant changes in the spectrum.

2. Orientational relaxation

Previously, we found that the orientational relaxation of $SeCN^-$ in bulk D_2O occurs on two time scales, each reflecting distinct processes.[43] The biexponential anisotropy decay of $SeCN^-$ in bulk D_2O (black points) is reproduced[43] in Fig. 2. The shorter time scale, 1.4 ps, results from wobbling-in-a-cone dynamics of the CN bond vector.[43,69] This form of orientational diffusion occurs within a restricted angular space represented by a cone of half angle 21.5°.

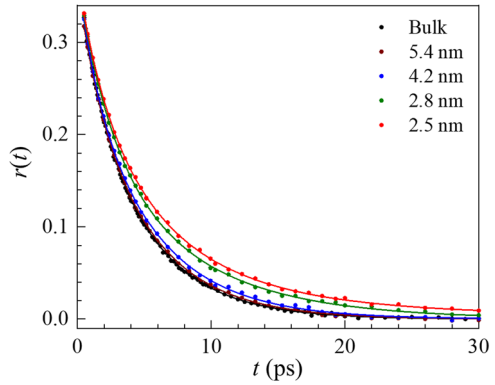

FIG. 2. Measured rotational anisotropy, $r(t)$, of $SeCN^-$ in bulk D_2O and in D_2O confined in silica pores of sizes 5.4 nm (brown curve), 4.2 nm (blue curve), 2.8 nm (green curve), and 2.5 nm (red curve). The solid curves are multiexponential fits to the data.

Complete randomization of the CN orientation occurs through small-step free diffusion on a second time scale of 4.5 ps, in a manner consistent with the Stokes–Einstein–Debye model.[43,70] In contrast, the anisotropy decay of HOD in D_2O, following a small extent of ultrafast inertial and librational motions, is single exponential with a time constant of 3 ± 0.2 ps[71] (2.6 ± 0.1 ps in H_2O[72]) and occurs through "jump" reorientation, in which multiple H-bonds are rapidly broken and reformed during large amplitude hydroxyl displacements of ~60°.[28,73] Although the reorientation mechanisms for $SeCN^-$ and HOD differ, the time scales of the motions are similar. This may be related to the fact that $SeCN^-$ engages in a similar number of H-bonds to water (~3.4)[43] as water engages in with itself (~3.5).[74] The rotation of both molecules is constrained by the dynamics that rearrange the H-bond network formed with surrounding water molecules.

The $SeCN^-$ experimental anisotropy decays are shown in Fig. 2 for the 5.4 nm (brown points), 4.2 nm (blue points), 2.8 nm (green points), and 2.5 nm (red points) silica pores. The orientational relaxation of $SeCN^-$ in confined D_2O becomes progressively slower as the pore diameter is reduced. The similarly colored solid curves are multiexponential fits to the data, and the fit parameters are given in Table III. The dynamics can be modeled as biexponential decays for all but the smallest pore size of 2.5 nm, which has a third low amplitude, slow component. Integrated correlation times, τ_c, which for multiexponential decays are the sum of the products of each amplitude and corresponding time constant,[18] are also given in Table III. These show that the confined dynamics slow significantly as the pore size becomes small but are very similar to the bulk liquid for the larger pore sizes.

From Table III, one might conclude that the first and second time constants exhibit a nonmonotonic trend in which they steadily slow, reaching their longest values by 2.8 nm, and then become faster as the pore size is further reduced to 2.5 nm. However, this seemingly complex trend is an artifact of the change in the functional form of the anisotropy from a biexponential to a triexponential as the slower $SeCN^-$ molecules near the silica surface become a larger contribution to the measured signal. As will be detailed in Secs. IV B 2 and IV C, the reorientation dynamics of $SeCN^-$ and water near the center of each pore remain bulk-like, while the dynamics near the surface are significantly slower. Even in the largest pore (5.4 nm), the $SeCN^-$ molecules near the surface rotate more slowly than the molecules in the pore interior, but they represent a very small contribution to the total signal, owing to their small number fraction. Thus, although $SeCN^-$ rotates on at least three distinct time scales in every size silica pore, only the two time scales associated with the molecules in the pore interior will be observed in very large pores. As the pore diameter decreases, the third time constant associated with interfacial $SeCN^-$ begins to emerge in the anisotropy decays. However, for intermediate pore sizes, the amplitude of the third component is small. The result is that the data can still be modeled with biexponential decays, but the amplitudes and time scales adjust to accommodate the emerging slow dynamics. This explains why the parameters t_1 and t_2 become longer as the pore size is reduced from 5.4 nm to 2.8 nm (Table III) but then accelerate at 2.5 nm where it becomes unambiguous that the decay is triexponential. In Sec. IV C, the time scales are more accurately determined by fitting the set of decay curves simultaneously with

TABLE III. Orientational relaxation parameters. Multiexponential fit parameters to the anisotropy for $SeCN^-$ in bulk D_2O and D_2O in silica pores of different sizes. A_i and t_i are the amplitude and time constant of the ith component. τ_c are integrated correlation times. The parameters for the bulk liquid and for the smallest pore size are reproduced with permission from Yamada *et al.*, J. Chem. Phys. **146**, 234501 (2017). Copyright 2017 AIP Publishing LLC and Yamada *et al.*, J. Phys. Chem. C **123**, 5790–5803 (2019). Copyright 2019 American Chemical Society, respectively.

	Sample	A_1	t_1 (ps)	A_2	t_2 (ps)	A_3	t_3 (ps)	τ_c (ps)
Expt.	Bulk	0.073 ± 0.002	1.4 ± 0.1	0.304 ± 0.003	4.5 ± 0.1			3.8 ± 0.1
	5.4 nm	0.07 ± 0.02	1.5 ± 0.3	0.29 ± 0.02	4.8 ± 0.1			4.1 ± 0.2
	4.2 nm	0.087 ± 0.01	1.3 ± 0.2	0.29 ± 0.01	5.1 ± 0.1			4.2 ± 0.2
	2.8 nm	0.17 ± 0.02	2.5 ± 0.2	0.20 ± 0.02	7.6 ± 0.3			5.3 ± 0.1
	2.5 nm	0.11 ± 0.04	2.0 ± 0.4	0.24 ± 0.03	6.2 ± 0.9	0.03 ± 0.02	25 ± 8	6.3 ± 0.5
Sim.	Bulk	0.1 ± 0.01	0.9 ± 0.1	0.29 ± 0.01	4.5 ± 0.1			3.5
	4.4 nm	0.14 ± 0.04	0.9 ± 0.3	0.26 ± 0.04	4.8 ± 0.6			3.6 ± 0.3
	2.4 nm	0.1 ± 0.02	0.6 ± 0.1	0.26 ± 0.03	4.8 ± 1.0	0.05 ± 0.04	20 ± 10	5.9 ± 1.0

a more complete physical description incorporating the $SeCN^-$ distributions and the radial dependence of the anisotropy determined in the simulations.

3. Spectral diffusion

While $SeCN^-$ and HOD reorient in a qualitatively different manner, their CN and OH stretches' spectral diffusion is directly comparable.[43] The spectral diffusion of the OH stretch of HOD in D_2O is characterized by two main time scales, 0.4 ± 0.1 ps and 1.4 ± 0.2 ps.[75,76] Very similar time scales are found for the OD stretch of HOD in H_2O, 0.4 ± 0.1 ps and 1.7 ± 0.2 ps.[72,77–79] The shorter time scale dynamics arise from local distance and angle fluctuations of intact H-bond configurations.[75–78] The longer spectral diffusion time scale has been shown through MD simulations to be caused by the complete randomization of the H-bond network structure, of which low concentration HOD is a non-perturbative component.[77,78] 2D IR experiments on $SeCN^-$ in bulk D_2O gave time constants of 0.6 ± 0.1 ps and 1.4 ± 0.2 ps.[43] There were small variations in the decay constants with polarization (parallel, perpendicular, and isotropic), which were within experimental error.[43] Here, the perpendicular polarization configuration (the polarizations of the pump pulses, pulses 1 and 2, were perpendicular to the polarizations of pulse 3 and the echo pulse) was used because it most effectively reduces the scattered light from the SiO_2 particles.[52]

2D IR spectra at time delays, T_w, of 0.5 ps and 5 ps are shown in Fig. 3 for bulk D_2O and for two of the confined D_2O systems. The red and blue bands are, respectively, the 1 ← 0 and 2 ← 1 vibrational transitions normally observed in third order optical experiments.[46] The spectral diffusion decay times and amplitudes were obtained using the center-line-slope (CLS) analysis[44,45] on the time-dependent 1 ← 0 band, as previously described.[18,43] The CLS decays are shown in Fig. 4 for $SeCN^-$ in bulk (black points) and confined D_2O in the 5.4 nm (brown points), 4.2 nm (blue points), 2.8 nm (green points), and 2.5 nm (red points) pores. As the pore size decreases, the CLS takes more time to fully decay. A possible interpretation is that the water H-bond network interacting with and surrounding $SeCN^-$ evolves more slowly with an increase in confinement. However, owing to the spatially averaged nature of the measurement, the apparent slowing with a decrease in pore size can alternatively result from a change in the relative signal contribution of molecules experiencing slow water structural rearrangements near the silica surface compared to those subject to bulk-like dynamics in the pore interior. In Sec. IV C, we demonstrate that the latter possibility is the appropriate description of the data.

The issues associated with interpreting independent multiexponential fits to the pore size-dependent anisotropy decays also apply to the CLS decays. However, multiexponential fits are useful for directly comparing the measured dynamics to the simulated results, and so, we present them for the CLS decays in Fig. 4 and Table IV. The multiexponential decays can be modeled with two time scales for the larger pores, but the 2.8 nm and 2.5 nm pores are better described with triexponential decays. As seen in the orientational relaxation dynamics, a significant increase in τ_c is observed in the transition from the 4.2 nm to 2.8 nm pore.

The CLS and linear absorption line shape were used to determine the FFCF,[44] which is given in Eq. (2). The τ_i are obtained directly from the CLS decay, while the frequency fluctuation amplitudes, Δ_i, are determined by reproducing the observed linear absorption line shape and CLS decay through response function calculations of the 1D and 2D line shapes.[44,80] The FFCF permits the

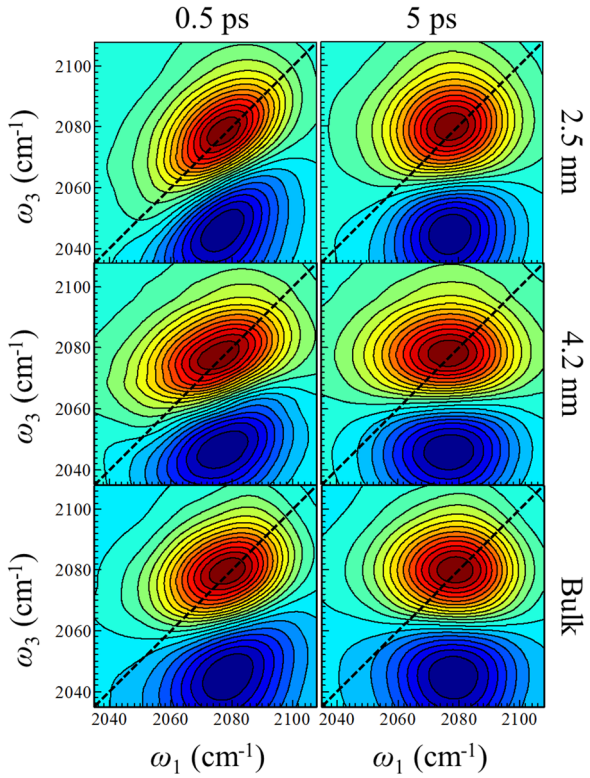

FIG. 3. 2D IR spectra of $SeCN^-$ in bulk D_2O and in D_2O confined in the 4.2 nm and 2.5 nm silica pores at time delays of 0.5 ps and 5 ps.

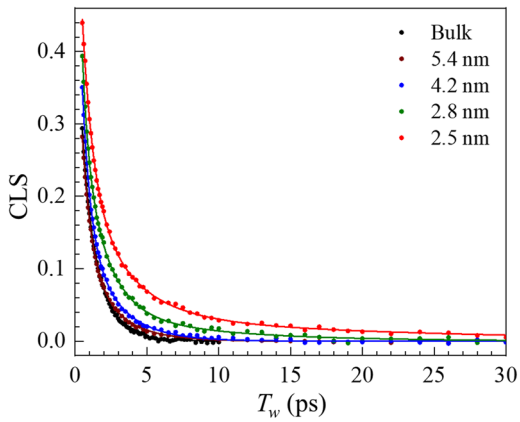

FIG. 4. Measured CLS decays (spectral diffusion) of $SeCN^-$ in bulk D_2O and in D_2O confined in silica pores of sizes 5.4 nm (brown curve), 4.2 nm (blue curve), 2.8 nm (green curve), and 2.5 nm (red curve). The solid curves are multiexponential fits to the data.

TABLE IV. CLS parameters. Multiexponential fit parameters to the CLS for $SeCN^-$ in bulk D_2O and D_2O in silica pores of different sizes. A_i and t_i are the amplitude and time constant of the ith component. τ_c are integrated correlation times. The parameters for the bulk liquid and for the smallest pore size are reproduced with permission from Yamada *et al.*, J. Chem. Phys. **146**, 234501 (2017). Copyright 2017 AIP Publishing LLC and Yamada *et al.*, J. Phys. Chem. C **123**, 5790–5803 (2019). Copyright 2019 American Chemical Society, respectively.

	Sample	A_1	t_1 (ps)	A_2	t_2 (ps)	A_3	t_3 (ps)	τ_c (ps)
Expt.	Bulk	0.22 ± 0.02	0.5 ± 0.1	0.30 ± 0.04	1.3 ± 0.2			0.97 ± 0.05
	5.4 nm	0.38 ± 0.01	0.65 ± 0.04	0.14 ± 0.02	2.3 ± 0.2			1.08 ± 0.06
	4.2 nm	0.48 ± 0.01	0.57 ± 0.03	0.19 ± 0.01	2.3 ± 0.1			1.05 ± 0.04
	2.8 nm	0.42 ± 0.02	0.41 ± 0.1	0.31 ± 0.02	1.7 ± 0.2	0.05 ± 0.01	8 ± 7	1.4 ± 0.1
	2.5 nm	0.49 ± 0.05	0.8 ± 0.2	0.19 ± 0.02	3.1 ± 0.3	0.04 ± 0.01	17 ± 1	2.4 ± 0.3
Sim.	Bulk	0.27 ± 0.01	0.6	0.11 ± 0.01	1.4	0.11 ± 0.01	6.9 ± 0.2	2.3
	4.4 nm	0.30 ± 0.01	0.6 ± 0.5	0.23 ± 0.01	6.7 ± 3.9	0.03 ± 0.01	54 ± 40	5.6
	2.4 nm	0.28 ± 0.01	1.7 ± 0.5	0.15 ± 0.01	10 ± 5	0.06 ± 0.01	60 ± 35	8.5

separation of spectral diffusion components that lie within the homogeneous or inhomogeneous limits, respectively, defined as satisfying $\Delta_i\tau_i \ll 1$ and $\Delta_i\tau_i \gg 1$.[46] In the homogeneous limit, the line shape is a Lorentzian of width $\Gamma = \Delta^2\tau/\pi = 1/\pi T_2$, where the experimentally observed homogeneous dephasing time is given by $(T_2)^{-1} = (T_2^*)^{-1} + (2T_1)^{-1} + (3T_{or})^{-1}$ (T_2^*, T_1, and T_{or} are the pure dephasing, vibrational, and orientational relaxation times, respectively). In the inhomogeneous limit, the line shape is a Gaussian with standard deviation Δ. The total inhomogeneous linewidth is then FWHM $= 2[2\ln(2)]^{1/2}\Delta_{\text{total}}$, where $\Delta_{\text{total}} = \left(\sum_i \Delta_i^2\right)^{1/2}$. The FFCF parameters obtained from the 2D IR experiments and simulation trajectories (discussed below) are displayed in Table V. Note that although Δ and τ cannot be independently determined experimentally for the homogeneous contribution to the line shape (hence, the tabulation of T_2 in Table V), this is not an issue in the simulations (Sec. IV B), for which the parameters are reported for all components of the FFCF. Note also that the FFCFs reported in Table V were obtained by treating the $SeCN^-$ dynamics as that of a single ensemble, as reported previously.[18] In Sec. IV B, it is shown that the spectral diffusion is well-described by a smoothed two-state model. However, it is not straightforward to decompose the dynamics into two FFCFs corresponding to core and shell $SeCN^-$ dynamics. The main issue is that the linear absorption spectrum varies continuously with distance from the silica interface and the spectra at all distances heavily overlap (see Sec. IV A). It is not possible to distinguish the shape of the spectrum in the interfacial layer from the experimental data. However, as shown in Sec. IV C, the CLS decay corresponding to $SeCN^-$ molecules in the interfacial layer can be determined.

B. Simulations

1. Linear IR spectra

Figure 5(a) displays the $SeCN^-$ linear absorption spectra, $I(\omega)$, calculated from the simulation trajectories for the bulk solution (black curve) and 4.4 nm (blue curve) and 2.4 nm (red curve) pores. The band centers and widths are shown in Table II. The simulations predict a <1 cm^{-1} redshift in the band centers relative to the bulk spectrum, which is consistent with the measurements (Fig. 1). However, the modeling overestimates, by ~60%, the width of the

TABLE V. FFCF parameters. T_2: Observed homogeneous dephasing time, $\Gamma = 1/\pi T_2$: Homogeneous linewidth, and Δ_i and τ_i: Frequency fluctuation amplitude and time constant for the ith component, respectively. The parameters for the bulk liquid and for the smallest pore size are reproduced with permission from Yamada *et al.*, J. Chem. Phys. **146**, 234501 (2017). Copyright 2017 AIP Publishing LLC and Yamada *et al.*, J. Phys. Chem. C **123**, 5790–5803 (2019). Copyright 2019 American Chemical Society, respectively.

	Sample	T_2 (ps)	Γ (cm^{-1})	Δ_1 (cm^{-1})	τ_1 (ps)	Δ_2 (cm^{-1})	τ_2 (ps)	Δ_3 (cm^{-1})	τ_3 (ps)
Expt.	Bulk	1.4 ± 0.1	8.7 ± 0.4	9.4 ± 0.5	0.5 ± 0.1	10.2 ± 0.9	1.3 ± 0.2		
	5.4 nm	1.2 ± 0.1	9.1 ± 0.8	12.1 ± 0.6	0.69 ± 0.03	5.8 ± 0.8	2.3 ± 0.4		
	4.2 nm	4 ± 1	2.5 ± 0.6	14.4 ± 0.2	0.57 ± 0.02	7.1 ± 0.1	2.3 ± 0.1		
	2.8 nm	8 ± 8	1.3 ± 0.9	11.9 ± 0.6	0.4 ± 0.1	9.9 ± 0.7	1.7 ± 0.2	3 ± 1	8 ± 7
	2.5 nm	2.3 ± 0.6	5 ± 1	12.2 ± 0.7	0.8 ± 0.2	6.8 ± 0.5	3.1 ± 0.3	3.1 ± 0.3	17 ± 1
	Sample	Δ_0 (cm^{-1})	τ_0 (ps)	Δ_1 (cm^{-1})	τ_1 (ps)	Δ_2 (cm^{-1})	τ_2 (ps)	Δ_3 (cm^{-1})	τ_3 (ps)
Sim.	Bulk	19.0 ± 0.1	0.089 ± 0.001	13.2 ± 0.1	0.6	6.0 ± 0.1	1.4	5.6 ± 0.1	7.1 ± 0.1
	4.4 nm	20.1 ± 2.4	0.10 ± 0.03	15.2 ± 2.0	0.6 ± 0.5	9.3 ± 5.3	6.7 ± 3.9	3.2 ± 2.6	54 ± 40
	2.4 nm	29.8 ± 0.9	0.157 ± 0.01	16.9 ± 1.0	1.7 ± 0.5	11.6 ± 1.5	10 ± 5	7.1 ± 2.6	60 ± 35

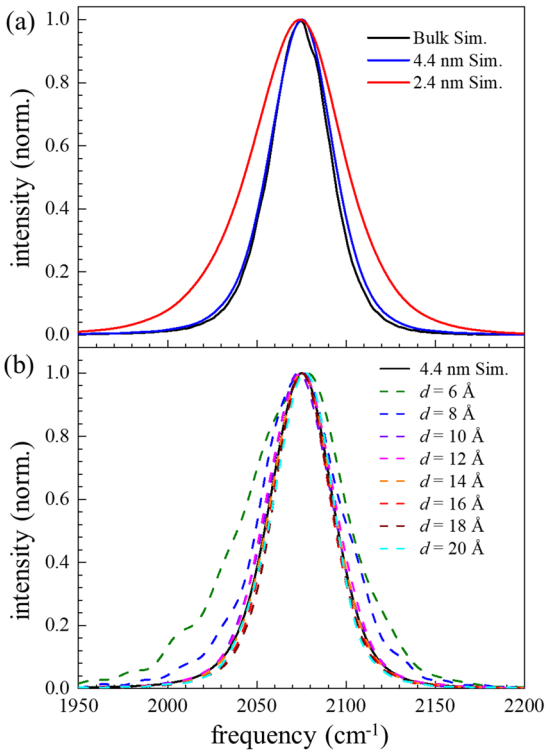

FIG. 5. (a) Simulated linear-IR spectra of $SeCN^-$ in D_2O: bulk (black curve), 4.4 nm pore (blue curve), and 2.4 nm pore (red curve). (b) Simulated linear-IR spectra for $SeCN^-$ in the 4.4 nm silica pore plotted as a function of the C atom distance to the nearest pore O atom, *d*.

spectrum in the smallest pore, which results from greater heterogeneity in the CN frequency distribution, $P(\omega) = \langle \delta(\omega - \omega_{01}) \rangle$, in the pore relative to the bulk (Table II). The disagreement with experiment for the $SeCN^-$ line shape in the 2.4 nm pores may be indicative of some shortcomings of the empirical mapping approach, as previously discussed in Ref. 18. The spectrum in the 4.4 nm pore model is only slightly broadened by ~2.5 cm^{-1} relative to the bulk spectrum, which is in better agreement with the experiments. The distribution of frequencies, $P(\omega)$, and the spectral density, $P_\mu(\omega) = \langle |\mu_{01}|^2 \delta(\omega - \omega_{01}) \rangle$, in the 4.4 nm pore are also very similar to those of the bulk (Table II).

In Fig. 5(b), the simulated spectrum in the 4.4 nm pore is decomposed according to the different $SeCN^-$ positions, *d*, defined as the distance of the C atom from the nearest pore O atom at $t = 0$ in the calculation of the response function.[18,43] Previously, in the 2.4 nm pore, the spectrum blue-shifted and narrowed with an increase in *d*.[18] By ~10 Å, the spectrum was very close to the bulk spectrum, displaying only a slightly broader linewidth. Like the 2.4 nm pore, in the 4.4 nm pore, increased linewidth is observed as $SeCN^-$ approaches the interface, but it is accompanied by a smaller change in the center position of the spectrum. In the 4.4 nm pore, $SeCN^-$ can access further distances from the interface, and it is clear that the spectrum continues to approach the bulk spectrum for increasing distances, *d*. Figure 5(b) further emphasizes the important distinction between this system and RMs or Nafion fuel-cell membranes: the linear absorption spectrum cannot be decomposed into a single "core" and "shell" spectrum. Rather, a range of spectra exist along the radius of the pore, and the observed spectrum results from the sum of these distance-dependent spectra weighted by the probability of finding $SeCN^-$ at different positions along the radial coordinate.

The distance-dependent spectra indicate the importance of the $SeCN^-$ position or rather its distribution of positions. The probability distribution for the C atom of the solute is plotted as a function of distance, *d*, from the nearest pore O atom in Fig. 6(a) for the 2.4 nm pore and in Fig. 6(b) for the 4.4 nm pore. The corresponding O_w and D_w atom distributions for D_2O are shown for comparison. In both cases, the solute explores a broad distribution of positions relative to the pore interface. A key feature, however, is that the $SeCN^-$ avoids the pore interface as represented by the strongly structured water indicated by the peaks in the O_w and D_w distributions at distances less than 4 Å. In the 2.4 nm pore, there is a small tail in the C atom position that extends to these small values of *d*; in the 4.4 nm pore, the solute is never observed in the interfacial region. (Given the significantly broader IR absorption spectrum predicted in the 2.4 nm pore simulations compared to the corresponding measurements, it is possible that the model overestimates the $SeCN^-$ density in the interfacial region for the smallest pore.) In both pores, the solute distribution peaks far from the interface with average values of *d* of 6.9 Å and 14 Å for the 2.4 nm and 4.4 nm pores, respectively. These results indicate that the $SeCN^-$ spectroscopy does not probe the interfacial layer of water that lies within a single molecular diameter of the silica surface. It will be interesting in future studies to examine other probes that may do so.

The influence of confinement on the $SeCN^-$ can also be evaluated in terms of its H-bonding. In studies of the solute in bulk D_2O, we previously observed that water–$SeCN^-$ H-bonds can be classified as axial (with a C–N··· D angle less than 120°) or equatorial (all other

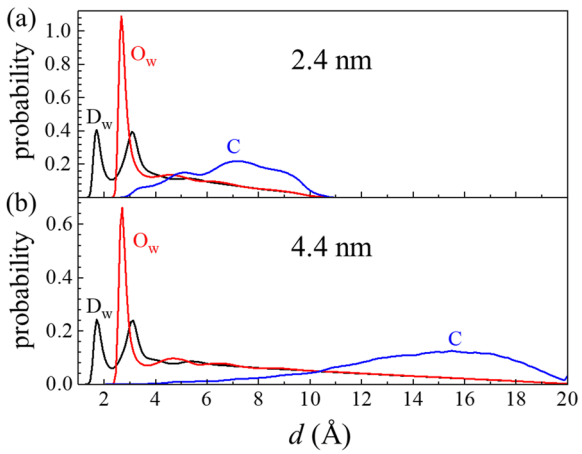

FIG. 6. Probability distribution for the $SeCN^-$ carbon atom (C, blue curve) and D_2O oxygen (O_w, red curve) and deuterium (D_w, black curve) atoms in the (a) 2.4 nm and (b) 4.4 nm pores.

H-bonds); the former are important because they generally give rise to a blueshift in the CN stretching frequency associated with charge transfer, while the latter lead to a redshift.[43,81,82] The distribution of the number of both axial and total (axial plus equatorial) H-bonds is given for $SeCN^-$ in D_2O in the bulk liquid, a 2.4 nm pore, and a 4.4 nm pore in Fig. 7(a). It is found that there are only slight changes to the distribution of axial H-bonds, with the 2.4 nm pore leading to slightly fewer. A larger, but still small, change is observed in the distribution of total H-bonds; both pores have a distribution skewed to fewer total H-bonds compared to the bulk with the effect greater in the 2.4 nm pore. These changes in the H-bond structure are further illustrated in Fig. 7(b), where the average number of total and axial H-bonds is plotted as a function of the distance of the C atom from the nearest pore O atom. The smallest number of total H-bonds is observed in the 2.4 nm pore, and the largest number (3.4) is found in the bulk liquid. The distance-dependence is weak with a moderate decrease seen at 3 Å, a distance that is not accessed by $SeCN^-$ in the larger pore, followed by a gradual decay as d is increased beyond 4 Å. The number of axial H-bonds also decreases with an increase in confinement but more weakly. There is no distance-dependence in the average number of axial H-bonds that is observable outside the statistical uncertainties.

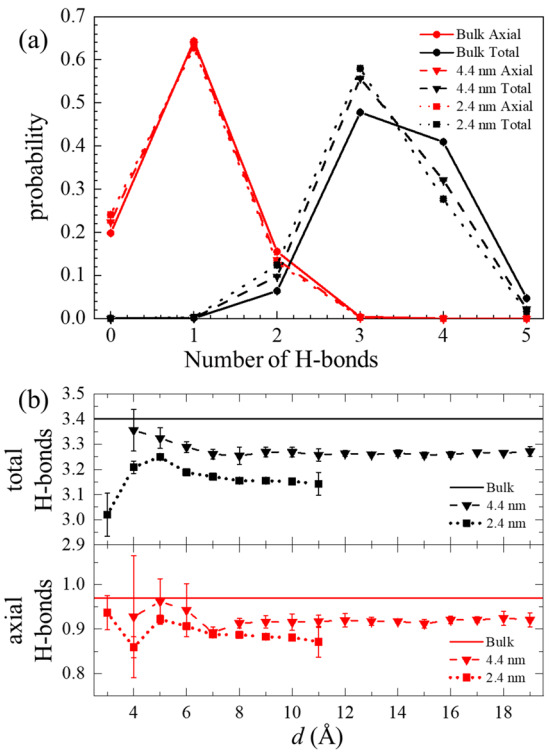

FIG. 7. (a) Probability of the total number of H-bonds donated to $SeCN^-$ by D_2O and silanols (black points) and the number of axial H-bonds (red points) defined as $\theta_{CND} \geq 120°$. Solid lines: bulk, dashed lines: 4.4 nm, and dotted lines: 2.4 nm. (b) Average number of total (black) and axial (red) H-bonds donated to $SeCN^-$ vs the C atom distance to the nearest pore O atom, d, in the 4.4 nm (dashed lines) and 2.4 nm (solid lines) pores. The bulk values from Ref. 43 (solid lines) are shown as horizontal lines.

It is interesting to also examine the connection between the H-bonds and the CN stretching frequency. This is done in Fig. 8(a) where the average fundamental vibrational frequency is plotted vs the number of total and axial H-bonds. As noted above, the axial H-bonds lead to blueshifts in the CN frequency, indicated by the positive slope in the average frequency with the number of axial H-bonds. The equatorial H-bonds induce redshifts, which accounts for the negative slope in the frequency with the total number of H-bonds. There is little change in the average frequency for a given number of H-bonds of either type, although slightly larger blueshifts are observed in the pores for a given number of axial H-bonds.

The average fundamental vibrational frequency as a function of the $SeCN^-$ distance from the pore surface is plotted in Fig. 8(b). The frequency modestly increases (blueshifts) with d before reaching a plateau around 6–8 Å. The frequencies are systematically higher for the 2.4 nm pore compared to the larger pore, which can be attributed to the smaller number of red-shifting equatorial H-bonds.

2. Orientational relaxation

In Fig. 9, the anisotropy, $r(t)$, of $SeCN^-$ in bulk and nanoconfined D_2O, for two pore sizes, is compared to the calculated anisotropies from the simulations. The calculation of $r(t)$ from the

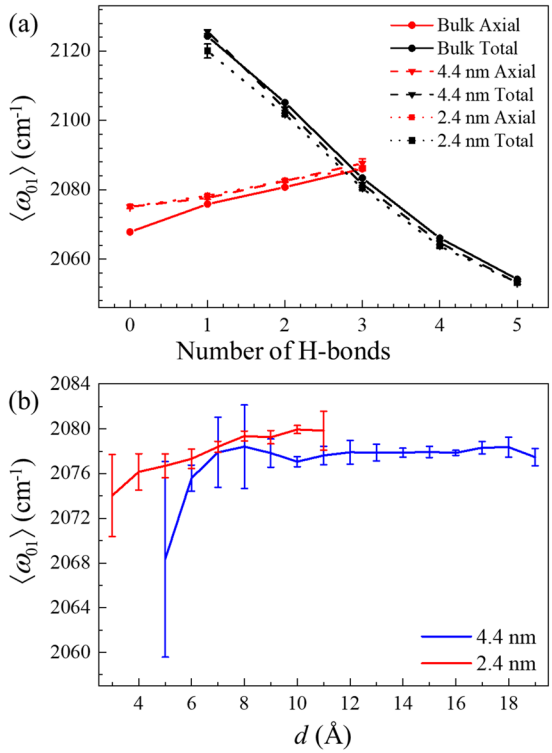

FIG. 8. (a) Average CN stretching frequency vs the number of total (black points) and axial (red points) H-bonds formed. Solid lines: bulk, dashed lines: 4.4 nm, and dotted lines: 2.4 nm. (b) Average CN stretching frequency as a function of d in the 4.4 nm (blue solid line) and 2.4 nm (red solid line) pores.

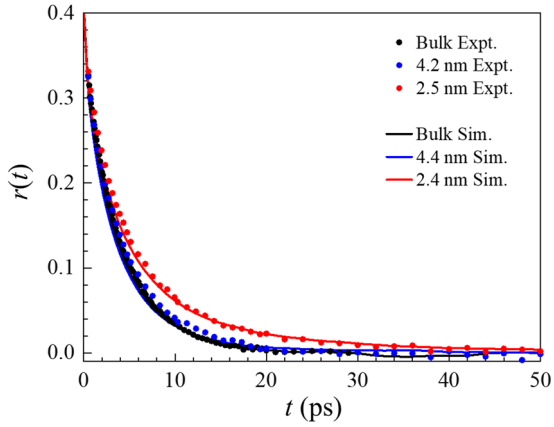

FIG. 9. Anisotropy, $r(t)$, decays for the bulk (black points), 4.2 nm pore (blue points), and 2.5 nm pore (red points) are compared to the simulated $r(t)$ for the bulk (black curve), 4.4 nm pore (blue curve), and 2.4 nm pore (red curve).

measured signals is given in Eq. (4). The calculation from the simulation trajectories was described in detail previously.[18,43] The data for the 4.2 nm (blue points) and 2.5 nm pore (red points) sizes are shown for comparison to the simulated dynamics in the 4.4 nm (blue curve) and 2.4 nm (red curve) pores. The measured and simulated dynamics for the bulk[43] and smallest pore[18] were reported previously. The agreement with the measurements is very good, indicating that the modeling captures the size dependence of the rotational dynamics accurately. The observed spatially averaged dynamics rapidly approach bulk dynamics for a pore radius increase of 0.85 nm, i.e., going from a radius of 1.25 nm (~5 water molecules) to 2.1 nm (~8 water molecules), an increase of ~3 water molecules. This occurs because the characteristic distance over which the interfacial dynamics transition to bulk dynamics is on the order of the size of the water molecule, which has been suggested by several previous studies.[10,13,23,28,83]

In a similar manner to the linear absorption spectrum, the simulated $SeCN^-$ anisotropy in the 4.4 nm pore is decomposed as a function of the distance, d, at $t = 0$ in Fig. 10(a). The anisotropy decay is slower when the $SeCN^-$ solute is closer to the pore interface and accelerates with an increase in d, until the dynamics converge to that observed in bulk D_2O.[43] The changes with d are further illustrated in Fig. 10(b), where the values of the decays of $C_2(t)$ at specific times between 1.2 ps and 4.8 ps are plotted as a function of d. The present results for the 4.4 nm pore are plotted along with those previously obtained for the 2.4 nm pore.[18] The results for the two pore sizes coincide. This coincidence demonstrates that the distance-dependence of the reorientational dynamics is independent of pore size and thus represents primarily an interfacial, rather than confinement, effect. For a given delay time, $SeCN^-$ exhibits reorientation that becomes faster exponentially with the distance from the pore interface. The length scale (correlation length, ξ) of this decay is ~2.2 Å, which is slightly smaller than the diameter of a single water molecule. Thus, the effect of the interface on the anisotropy decay is short-ranged and is most prevalent very close to the surface.

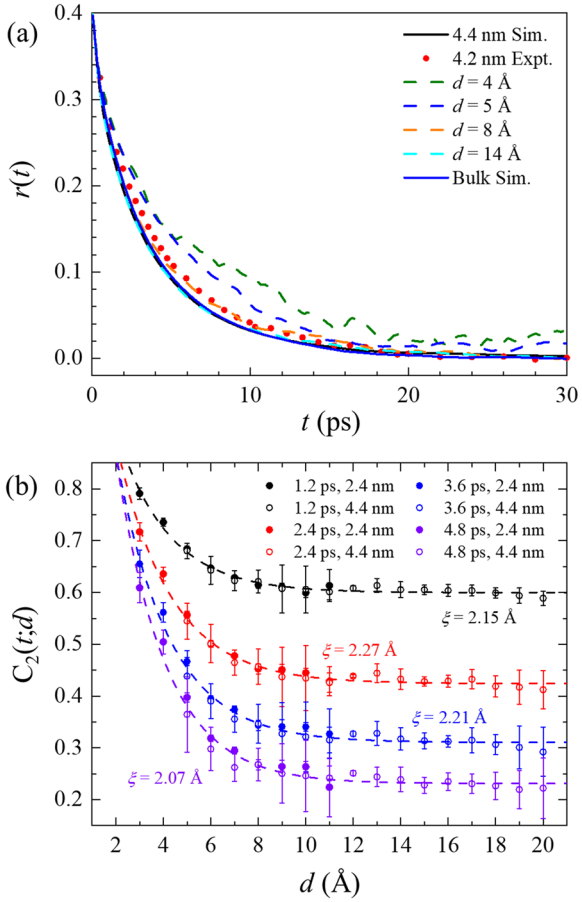

FIG. 10. (a) Simulated $r(t)$ analyzed as a function of the distance between the C atom and the nearest pore O atom, d, for the 4.4 nm silica pore. The measured data for the 4.2 nm pore (red points) are shown for comparison. (b) Simulated $C_2(t;d)$ as a function of the distance, d, evaluated for the model 2.4 nm (solid points) and 4.4 nm silica pores (open points) at four delay times: 1.2 ps (black), 2.4 ps (red), 3.6 ps (blue), and 4.8 ps (violet). Dashed lines of the same color show simultaneous fits of an exponential decay to both datasets. The resulting correlation length, ξ, is displayed for each time delay.

3. Spectral diffusion

The spectral diffusion dynamics were also predicted through the simulation of the FFCF. The FFCF simulation is fundamentally different from simulating the orientational relaxation. Simulation of the orientational relaxation is performed for the vibrational ground state and is straightforward using a classical MD simulation. A vector along the transition dipole direction is tracked as a function of time, and $C_2(t)$ is determined.[18,43] The FFCF is a measure of the transition frequency fluctuations, which is quantum mechanical. Methods have been developed for obtaining the FFCF from a classical simulation[80] and specifically for the systems studied here.[18,43] The simulations provide important insights into H-bond dynamics in the mesopores but do not produce the level of agreement with experiment obtained in the orientational relaxation simulations discussed above.

In Fig. 11, the measured CLS decays for the bulk (black points), 4.2 nm pore (blue points), and 2.5 nm pore (red points) are compared to the computed CLS decays (dashed curves) obtained from nonlinear response function calculations using the simulated FFCFs.[18,43] The simulations capture the observed trend of slowing water H-bond fluctuations as the confinement becomes more extreme; however, the degree of slowing is overestimated in the modeling. The simulations also predict a slower approach to bulk dynamics as the pore size is increased than observed in the measurements. Table IV also lists the parameters obtained from the multiexponential fits to the simulated CLS decays.

The simulated spectral diffusion dynamics are further analyzed in Fig. 12(a), where the FFCF is plotted as a function of the distance, d. As with the anisotropy decay, the spectral diffusion accelerates with the $SeCN^-$ distance from the pore surface and exhibits dynamics identical to that in bulk D_2O[43] in the pore interior. This distance-dependence is examined in greater detail in Fig. 12(b) in which the FFCF is plotted at particular times as a function of the initial distance d of the $SeCN^-$ probe. The simulations for the 4.4 nm pore are shown along with those for the 2.4 nm pore,[18] and the results are in agreement. The distance-dependences of the spectral diffusion dynamics are qualitatively different from those for the reorientational anisotropy shown in Fig. 10. In particular, the FFCF is well described by a smoothed step function, indicative of the two-state model behavior. The spectral diffusion occurs with bulk-like dynamics away from the interface and with modified dynamics in a layer very close to the surface that is the same independent of the $SeCN^-$ location within this layer, although the layer width is just slightly bigger than one water molecule.

C. Modifications to the two-state model: Scaling of dynamics with size

In this section, we present an analytical model of the confined water dynamics sensed by $SeCN^-$ and the change in the dynamics with an increase in pore radius. Insights from the simulations are used where possible to reduce the number of assumptions invoked to model the dynamics. A key result from the simulations, which is satisfied by the anisotropy [Fig. 10(b)] and spectral diffusion [Fig. 12(b)], is that the distance-dependence of the dynamics is independent of the pore radius for the investigated range of sizes. This result suggests that it is possible to model the experimental data presented below with a single interfacial (shell) and core correlation function.

Making the reasonable approximation of cylindrical symmetry for the pore system, the spatial aspects of the confinement are described by the radial dependence of the dynamical properties. Let R denote the radius of the pore. The radial distance from the

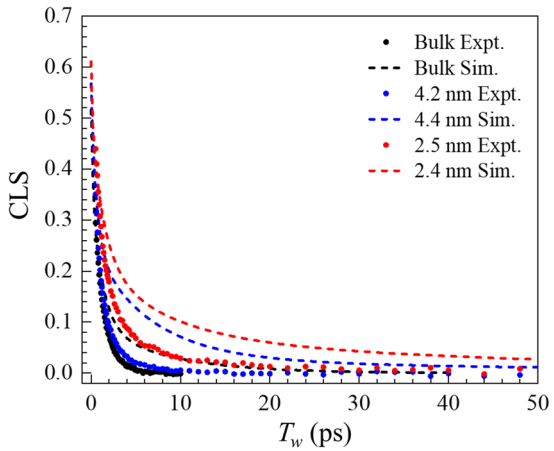

FIG. 11. CLS decays for the bulk (black points), 4.2 nm pore (blue points), and 2.5 nm pore (red points) are compared to the simulated CLS decays for the bulk (black dashed curve), 4.4 nm pore (blue dashed curve), and 2.4 nm pore (red dashed curve).

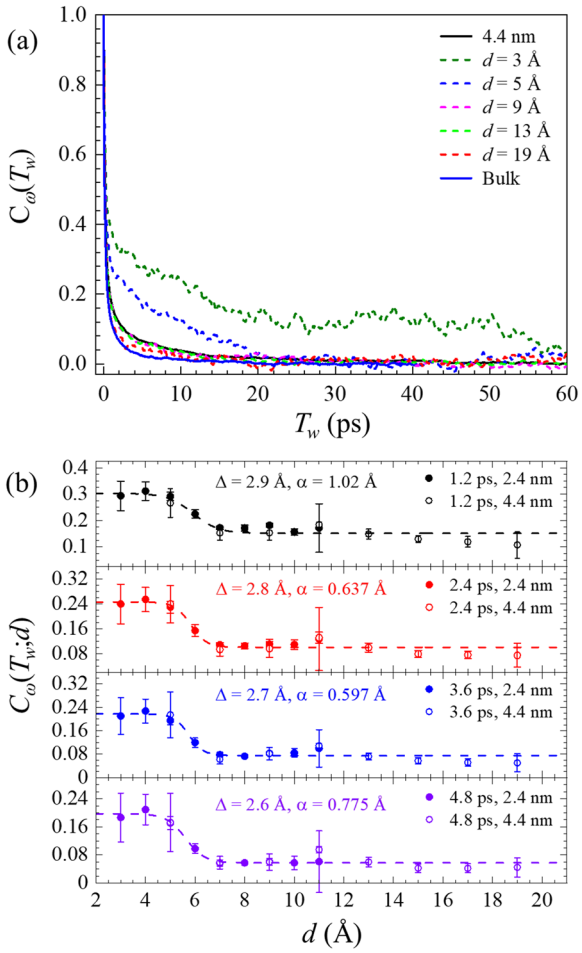

FIG. 12. (a) Simulated normalized FFCF as a function of the distance, d, between the C atom and the nearest pore O atom (dashed curves) compared to the total normalized FFCF for the 4.4 nm model pore (black solid curve) and bulk solution (blue solid curve). (b) Simulated normalized FFCF as a function of the distance, d, evaluated for the 2.4 nm (solid points) and 4.4 nm silica pores (open points) at four delay times: 1.2 ps (black), 2.4 ps (red), 3.6 ps (blue), and 4.8 ps (violet). Dashed lines of the same color show simultaneous fits of a smoothed step function to both datasets.

center of the pore, ρ, and the distance from the pore surface, d, are then related by $R = \rho + d$.[84] The simulations show that the radial dependence of the reorientational dynamics can be expressed as an exponential decay model [Figs. 10(b) and 13(a)],

$$r(t;\rho) = r_{2,\mathrm{core}}(t) + [r_{2,\mathrm{shell}}(t) - r_{2,\mathrm{core}}(t)]e^{-(R-d_0-\rho)/\xi}, \quad (5)$$

where ξ is the characteristic length of the exponential and d_0 is a reference distance. In contrast, a smoothed two-state model describes the spectral diffusion dynamics [Figs. 12(b) and 13(b)],

$$\mathrm{CLS}(t;\rho) = \mathrm{CLS}_{\mathrm{core}}(t) + [\mathrm{CLS}_{\mathrm{shell}}(t) - \mathrm{CLS}_{\mathrm{core}}(t)] \times \frac{\tanh[\{\Delta - (R - d_0 - \rho)\}/\alpha] + 1}{2}, \quad (6)$$

where Δ is the width of the interfacial layer and α is a parameter that determines the smoothness of the step transition. To compute the spatially averaged property for pore size, R, the radial-dependent dynamical property, $P(t;\rho)$, weighted by the probability of finding the $SeCN^-$ molecule between ρ and $\rho + d\rho$, $f(\rho)d\rho$, is integrated over the entire pore,

$$P(t;R) = \int_0^R P(t;\rho)f(\rho)d\rho. \quad (7)$$

For each pore size, we select one of two forms for the probability density,

$$f(\rho) = A\rho^a \sin^2[\pi\rho/(R - d_0)] \times \theta[R - d_0 - \rho] \quad (8a)$$

or

$$f(\rho) = B(R - d_0 - \rho)^b \sin^2[\pi\rho/(R - d_0)] \times \theta[R - d_0 - \rho], \quad (8b)$$

where $a \geq 0$ and $b \geq 0$ are parameters that skew the distributions [Eq. (8a) or (8b)] to lean closer to the pore surface or closer to the pore center, respectively; θ is the Heaviside step function; and A and B are normalization constants that satisfy $\int_0^R f(\rho)d\rho = 1$. Note that

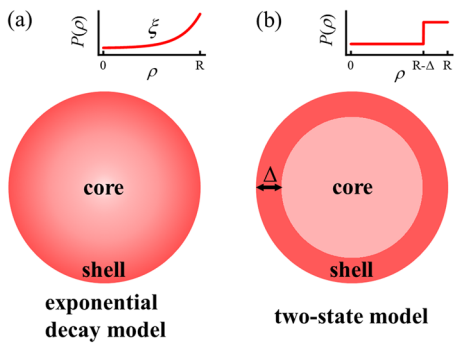

FIG. 13. (a) Exponential decay model with characteristic length ξ. The dynamical property $P(\rho)$, where ρ is the distance from the center of the pore, varies continuously from the core to shell value. (b) Two-state model with shell thickness Δ. $P(\rho)$ transitions from the core to shell value through a rapid step.

for $a = 0$ and $b = 0$, the probability densities are identical and peaked halfway between $\rho = 0$ and $\rho = R - d_0$.

The choice of the functions [Eqs. (8)] was informed by the calculated probabilities in the two model pores (Fig. 6), which are asymmetric and peaked at a distance away from the pore surface. These functions are not unique choices. However, it is important to select between surface- [Eq. (8a)] and center-leaning [Eq. (8b)] distributions in the fit to the data because, as determined in the simulations, the C atom probability distribution in the 4.4 nm pore [Fig. 6(b)] is more biased toward the pore center compared to that in the smaller 2.4 nm pore [Fig. 6(a)]. As seen in Fig. 6(a), the probability of finding the C atom of $SeCN^-$ at a distance, d, away from the surface has several local maxima. The fine structure in the probability density from the simulations is not straightforward to model with simple functions. Only the major features of the distributions and dynamics from the simulations were retained in the present description.

The parameters d_0, ξ, Δ, and α appearing in Eqs. (5) and (6) were fixed to values obtained from the analysis of the simulations. The reference distance, d_0, was set to 3 Å. As seen in Figs. 10(b) and 12(b), independent fits to the dynamic properties at different time delays result in modest differences in the parameters ξ, Δ, and α, which indicates that the distance-dependence of each amplitude and time scale in the multiexponential decays is not quite the same. However, because the differences are small, their values were determined again by sharing them in the fits in Figs. 10(b) and 12(b). The values obtained were $\xi = 2.0$ Å, $\Delta = 2.8$ Å, and $\alpha = 0.75$ Å. The effect of having a small distribution of pore sizes could also be included, but given the narrowness of the distributions (Table I), this effect is not significant.

The anisotropy and spectral diffusion decays for the bulk and confined liquid in the series of pores were globally fit using the above parameters. A size-independent core and shell correlation function was varied to fit all decay curves for each observable. The correlation functions were modeled as multiexponential decays, and the minimum number of exponentials needed to obtain agreement with the data was used. Improved agreement with the long time spectral diffusion data was obtained by fixing the slowest interfacial spectral diffusion time scale in the model to the slowest time constant (14.6 ps) shared across tri-exponential fits to the CLS decay curves (the first and second time constants in these fits were not fixed). The core dynamics were assumed to be identical to the bulk dynamics in the fitting. This choice is supported by the spatial decomposition of the time correlation functions (TCFs) in the 2.4 nm[18] and 4.4 nm silica pores [Figs. 10(a) and 12(a)]. By a distance of ~10 Å from the surface of either pore model, the $SeCN^-$ dynamics are nearly identical to the dynamics in bulk D_2O. For each pore size, R, a single probability distribution that produced the best agreement with the data was used. The fits (solid curves) to the data (solid points) are shown in Fig. 14. The core and interfacial parameters extracted from the fit to the experimental data are displayed in Table VI. Also shown are the predicted interfacial dynamics (dashed magenta curves). The $SeCN^-$ probability distributions are shown in Fig. 15.

As seen in Fig. 14, the calculated anisotropy and CLS decays reproduce the full time-dependence of the measured decays quite well for the bulk liquid and all pore sizes. The interfacial and core correlation functions are independent of ρ in Eqs. (5) and (6);

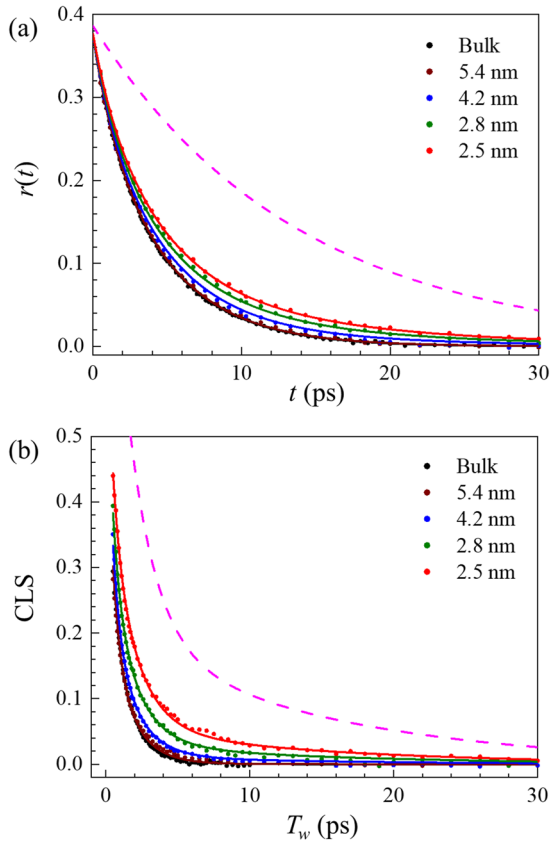

FIG. 14. (a) Measured rotational anisotropy, $r(t)$, and (b) CLS decays (spectral diffusion) of $SeCN^-$ in bulk D_2O (black points) and D_2O confined in silica pores of sizes 5.4 nm (brown points), 4.2 nm (blue points), 2.8 nm (green points), and 2.5 nm (red points). The solid curves of the same color are model fits to the data as described in the text. The magenta dashed curves are the interfacial (shell) dynamics that yield the best fit to the complete series of pore sizes.

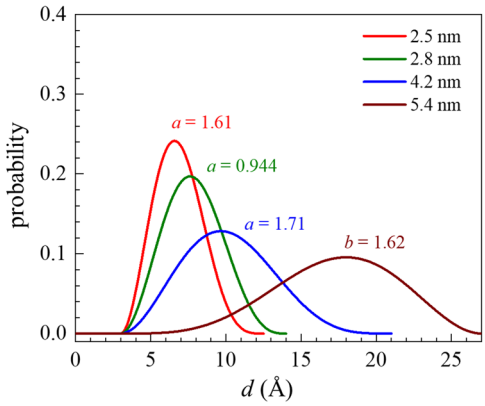

FIG. 15. Probability distributions, obtained from fits to the measured dynamics, for finding $SeCN^-$ at different distances, d, from the interface of different size silica pores: 2.5 nm (red), 2.8 nm (green), 4.2 nm (blue), and 5.4 nm (brown).

therefore, the averaged quantities, $r(t; R)$ and $CLS(t; R)$, are linear combinations of them. The core anisotropy is biexponential with time constants of 1.3 ps and 4.5 ps, while the shell anisotropy is sufficiently modeled as a single exponential with a time constant of 14 ps. As R decreases and the confinement becomes more extreme, the contribution of the interfacial correlation function to the decay increases, while that of the core decreases. The two components in the core are readily identified with bulk wobbling-in-a-cone dynamics and free orientational diffusion of the CN transition dipole moment, as discussed in Sec. IV A 2. A single slow relaxation in the interfacial dynamics is obtained from the fit, suggesting that the wobbling motions normally observed under bulk conditions are low in amplitude, or potentially absent, near the silica surface. Similarly, the presence of distinct wobbling motions of $SeCN^-$ near the interface of RMs could not be detected, nor could they be definitively excluded.[16]

TABLE VI. Core and interfacial dynamics from experimental data.

	A_1	t_1 (ps)	A_2	t_2 (ps)
$r_{core}(t)$	0.07 ± 0.01	1.3 ± 0.2	0.31 ± 0.1	4.5 ± 0.2
$r_{shell}(t)$	0.39 ± 0.01	14 ± 1		
$CLS_{core}(t)$	0.37 ± 0.05	0.5 ± 0.1	0.22 ± 0.05	1.6 ± 0.2
$CLS_{shell}(t)$	0.80 ± 0.04	1.9 ± 0.4	0.20 ± 0.05	14.6[a]

[a]This value was fixed in the fitting.

We previously found that the simulated rotational dynamics at $d = 3$ Å in the 2.4 nm pore model were fit well with a triexponential decay, although the error was significant, owing to the limited sampling of the interfacial dynamics.[18] The time constants 0.4 ps, 9.2 ps, and 37 ps represent approximately 15%, 48%, and 37% of the decay, respectively. The 0.4 ps observed in the simulations reflects motions intermediate between inertial and wobbling-in-a-cone orientational sampling. The dominant component, 9.2 ps, is quite similar to the 14 ps experimental time scale extracted from the exponential decay model. The 37 ps component is longer than any time scale determined in the experiments, and it may be less reliable, owing to the error at later times in the simulated interfacial dynamics. Considering the difficulty in establishing these values, it may be the case that a time intermediate between 9.2 ps and 37 ps in the simulations is reflective of the single 14 ps interfacial component extracted from the analytical model fit to the data.

That the data can be successfully modeled with a size-invariant $r(t; d)$ [Eq. (5) is independent of R after substituting $R = \rho + d$] is notable, considering simulations of RMs in the size range ~1.7 nm to ~3.3 nm, which found that the anisotropy as a function of distance from the interface becomes slower as the micelle becomes smaller.[13] The precise reasons for this behavior remain unclear, but several explanations have been suggested, including curvature-induced frustration or changes in interface structure and surface charge density with size.[13] In the pores studied here, nanoconfinement is in two dimensions in contrast to RMs in which water is nanoconfined in three dimensions. Because the confinement is effectively weaker in the silica pores, it is possible that the dynamics only

become dependent on the radius for extremely narrow pores below the smallest size (2.5 nm) studied here.

The rotational dynamics of $SeCN^-$ in silica confined water do not follow two-state behavior. The conventional two-state model assumes that the dynamics in the core and shell regions of the nanostructure are homogeneous.[17,33] Although the interfacial and core dynamics remain essentially constant as a function of silica pore size, the transition between these two limits follows an exponential distance-dependence [Fig. 10(b)]. Thus, a range of states (rather than just two), which are a combination of interface-like and core-like rotational dynamics, exist along the radius of the pore. The simulation work on RMs also found that the rotational correlation function decayed exponentially with distance from the surface, although only RMs smaller than ~3.3 nm were analyzed.[13] Increasing evidence indicates that the basic assumption of *homogenously distributed* core and shell dynamics does not apply in the case of RMs, regardless of size.[14] In other words, the ability to decompose the measured dynamics into "core" and "shell" time scales does not necessarily describe the spatial distribution of these time scales in the nanostructures.

It is interesting to then consider why the onset of slowing occurs at larger diameters in RMs.[16] If one neglects differences in interfacial chemistry, a possible explanation would be that it is a geometrical effect. This can be understood by considering a cylinder and a sphere both of radius R. For simplicity, if we assume that $SeCN^-$ is uniformly distributed in both geometries, its probability distributions are $f_{\text{cylinder}}(\rho) = 2\rho/R^2$ and $f_{\text{sphere}}(\rho) = 3\rho^2/R^3$ for the cylinder and sphere, respectively. This gives $f_{\text{sphere}}/f_{\text{cylinder}} = 3\rho/2R$, which says that for $\rho > 2R/3$, $f_{\text{sphere}} > f_{\text{cylinder}}$. Thus, $SeCN^-$ will sample the slower dynamics near the interface of a sphere to a greater extent than those near the interface of a cylinder of equivalent radius. However, we know from the current study that $SeCN^-$ is not uniformly distributed in the silica pores (Fig. 6), and uniformity is unlikely in RMs as well.[16,85] The $SeCN^-$ distributions are also likely strongly dependent on the nature of the surfactant head group. More information on the spatial distribution of the probe molecules in different nanoconfined systems is necessary to make quantitative comparisons of this type.

In contrast to the rotational dynamics, both the core and interfacial correlation functions for the CLS are biexponential. The time constants are 0.50 ps and 1.6 ps for the core, and 1.9 ps and 14.6 ps for the shell. However, because the longer core time constant and the shorter shell time constant are similar, they will appear as a single time whose amplitude in the decay is determined by the pore size, R. Thus, the decay will appear very close to a triexponential, which is consistent with the original multiexponential fits to the 2.8 nm and 2.5 nm pore data (Tables IV and V). The two core time scales correspond to small distance and angle fluctuations of intact H-bonds and changes in the H-bond arrangements that are faster than H-bond switches, respectively.[43] We consider two possible interpretations of the interfacial spectral diffusion. One possibility is that the 1.9 ps component corresponds to the slower H-bond fluctuations at the interface, and the 14.6 ps component represents a slower process of unknown origin. However, this would mean that H-bond dynamics near the silica interface are virtually unchanged from those in the bulk liquid; previous simulations have found that H-bond exchange slows by a factor of two or more at the silica pore interface.[28,83] A more reasonable interpretation instead views the interfacial time scales as slower analogs of the core components. These results suggest that the H-bond dynamics at 3 Å from the silica surface are ~9-fold slower than in bulk water.

Similarly, the spectral diffusion dynamics of tricyanomethanide (TCM) anions in the water pools of RMs were modeled as a function of the RM size.[14] In this model, the TCM anion was assumed to be uniformly distributed in the RM spherical water pool, the interfacial and core time constants were taken to be independent of the size of the RM, and the spectral diffusion correlation time was assumed to accelerate exponentially with distance from the interface. An exponential form was chosen based on simulations that demonstrated that the *rotational dynamics* of water exhibit this behavior in RMs.[13] However, the correlation time could not be adequately modeled with these assumptions.[14] Improved agreement was obtained after the authors further assumed that the characteristic length of the decay increased exponentially as the RM became smaller. We have also found that the rotational dynamics of $SeCN^-$ decay exponentially with distance from the surface of mesoporous silica [Fig. 10(b) and Eq. (5)]. However, as shown in Fig. 12(b), the spectral diffusion dynamics of $SeCN^-$ decay as a smoothed step-function [Eq. (6)] rather than an exponential. The smoothness of the step is determined by the parameter $\alpha = 0.745$ Å. The smaller its value, the closer the Eq. (6) comes to representing an instantaneous step. Larger values of α indicate a breakdown of the assumption of homogeneous dynamics accompanied by a sharp transition between core and shell regions. The width of the step transition is similar to the size of a water molecule [Fig. 12(b)]. In previous studies, a step-function reproduced the spectral diffusion amplitudes of a silane probe on the surface of spherical silica mesopores of varying size[32] and was also used in a three-layer model of the dielectric relaxation time distributions of H-bond forming diols confined in sol–gel glasses.[7] Additional simulation work is needed to elucidate the dependence of spectral diffusion on the distance from the interface of RMs and other nanoscale systems.

Finally, it is informative to consider the $SeCN^-$ probability distributions obtained from the fit to the data (Fig. 15). For the three smallest pore sizes, the distributions are biased toward the pore interface. The degree to which the distributions lean toward the interface is determined by the magnitude of the parameter a. The change in the parameter a with pore size is non-monotonic, reaching a minimum for the 2.8 nm pore. In contrast, the probability distribution for $SeCN^-$ in the 5.4 nm pore is biased toward the pore interior, which is reflected in the parameter $b = 1.62$ [Eq. (8b)]. This result is consistent with the results from the simulations showing that, as the pore radius increases, $SeCN^-$ spends more time away from the interface.

V. CONCLUDING REMARKS

The dynamics of water confined in mesoporous silica have been examined through analysis of the vibrational spectroscopy of the CN stretch of $SeCN^-$ dissolved in pores of varying diameters. FT-IR, PSPP, and 2D IR spectroscopy experiments were performed on four pore sizes from 5.4 nm down to 2.5 nm (the 2.5 nm pore was presented previously[18]). The three observables measured

with these methods are, respectively, linear absorption, orientational relaxation, and spectral diffusion. Identical measurements on $SeCN^-$ in bulk D_2O were presented in a previous publication[43] and are compared to the present results on the confined systems. Bulk water and two pore sizes, 2.4 nm and 4.4 nm, were investigated with MD simulations and closely compared to the measurements. The simulated dynamics in bulk solution[43] and the 2.4 nm pore[18] were recently reported. Simulations performed here for a 4.4 nm model silica pore elucidated the pore size-dependence of the observables.

The simulations show that the linear absorption line shape of $SeCN^-$ cannot be described as a sum of "core" and "shell" spectra, in contrast to that of HOD and $SeCN^-$ in RMs[11,15] and Nafion fuel-cell membranes.[66] The orientational relaxation and spectral diffusion of $SeCN^-$, measured as a function of pore size, exhibit different dependences on distance from the silica interface. Orientational relaxation is slow near the pore surface, speeds up with an exponential distance dependence as the distance from the surface increases, and becomes bulk-like when the distance is sufficiently large. In contrast, spectral diffusion is described by a smoothed step function. These results show that the two-state model is a more appropriate description of spectral diffusion, which is dominated by fluctuations of the water H-bond network in the vicinity of the probe. The distance-dependence of both quantities is independent of the pore size, indicating that the interface curvature has little influence on the dynamics of the range of sizes investigated, in agreement with previous simulation studies.[10,23,27] The characteristic length of the exponential decay, $\xi \sim 2$ Å, and the width of the interfacial region, $\Delta \sim 2.8$ Å, are similar to the diameter of a single water molecule. This correspondence between the size of the liquid molecule and the characteristic distances may be a more general feature of "ordinary" confined liquids. The $SeCN^-$ distributions in the silica pores are also found to be strongly non-uniform, exhibiting maxima far away from the silica interface. The distribution of the probe in the nanostructure plays a non-negligible role in the explication of the interfacial dynamics and was carefully considered in the analysis.

The orientational relaxation of $SeCN^-$ near the surfaces of silica and "large" RMs[16] is identical within the experimental uncertainties. This result, and the observation of confinement effects in spherical RMs for diameters that would yield bulk dynamics in cylindrical silica pores,[16] suggests that geometry also controls the size at which confinement begins to be manifested in the measurements. To form more rigorous comparisons, the $SeCN^-$ distributions and the distance-dependence of the anisotropy in RMs should be further explored. Previously, the spectral diffusion of anions in RMs[14] and IL thin films[21] was treated with an exponential decay model. In contrast, the present findings support a two-state picture of the spectral diffusion. The simulation of spectral diffusion in these other nanostructures can clarify whether this two-state behavior breaks down in other systems or is more general. Several studies also suggest that the interfacial dynamics and characteristic lengths in "small" RMs (~4 nm and smaller) depend on the RM size,[13,14] and it has been suggested that this could be observed in silica pores less than 1–2 nm in diameter.[23] The scaling of dynamical properties with size in this extreme confinement regime is not well-understood. Though highly desirable, a model that describes the full range of sizes has not yet been developed.

SUPPLEMENTARY MATERIAL

See the supplementary material for pore size distributions, isotropic pump-probe signals, vibrational lifetimes, simulated anisotropy with finer d resolution, and simulated normalized FFCF with finer d resolution.

ACKNOWLEDGMENTS

This work was funded by the Division of Chemical Sciences, Geosciences, and Biosciences, Office of Basic Energy Sciences of the U.S. Department of Energy through Grant Nos. DE-FG03-84ER13251 (S.A.Y. and M.D.F.) and DE-SC0019488 (W.H.T.). S.T.H. was supported by the National Science Foundation through the CCI program, No. CHE-1740645. Additional support of the 2D IR instrument and for M.D.F. was provided by the Air Force Office of Scientific Research, Grant No. FA9550-16-1-0104. The simulations were carried out at the University of Kansas Center for Research Computing (CRC). S.A.Y. gratefully acknowledges the support from a Stanford Graduate Fellowship.

REFERENCES

[1] A. M. Burke, J. P. Hanrahan, D. A. Healy, J. R. Sodeau, J. D. Holmes, and M. A. Morris, "Large pore bi-functionalised mesoporous silica for metal ion pollution treatment," J. Hazard. Mater. **164**, 229–234 (2009).
[2] D. P. Serrano, G. Calleja, J. A. Botas, and F. J. Gutierrez, "Adsorption and hydrophobic properties of mesostructured MCM-41 and SBA-15 materials for volatile organic compound removal," Ind. Eng. Chem. Res. **43**, 7010–7018 (2004).
[3] S. A. Didas, M. A. Sakwa-Novak, G. S. Foo, C. Sievers, and C. W. Jones, "Effect of amine surface coverage on the Co-adsorption of CO_2 and water: Spectral deconvolution of adsorbed species," J. Phys. Chem. Lett. **5**, 4194–4200 (2014).
[4] H. Ikemoto, Q. Chi, and J. Ulstrup, "Stability and catalytic kinetics of horseradish peroxidase confined in nanoporous SBA-15," J. Phys. Chem. C **114**, 16174–16180 (2010).
[5] B. Menaa, Y. Miyagawa, M. Takahashi, M. Herrero, V. Rives, F. Menaa, and D. K. Eggers, "Bioencapsulation of apomyoglobin in nanoporous organosilica sol–gel glasses: Influence of the siloxane network on the conformation and stability of a model protein," Biopolymers **91**, 895–906 (2009).
[6] S. Minakata and M. Komatsu, "Organic reactions on silica in water," Chem. Rev. **109**, 711–724 (2009).
[7] W. Gorbatschow, M. Arndt, R. Stannarius, and F. Kremer, "Dynamics of H-bonded liquids confined to nanopores," Europhys. Lett. **35**, 719–724 (1996).
[8] A. M. Dokter, S. Woutersen, and H. J. Bakker, "Inhomogeneous dynamics in confined water nanodroplets," Proc. Nat. Acad. Sci. U. S. A. **103**, 15355–15358 (2006).
[9] I. R. Piletic, D. E. Moilanen, D. B. Spry, N. E. Levinger, and M. D. Fayer, "Testing the core/shell model of nanoconfined water in reverse micelles using linear and nonlinear IR spectroscopy," J. Phys. Chem. A **110**, 4985–4999 (2006).
[10] S. R.-V. Castrillón, N. Giovambattista, I. A. Aksay, and P. G. Debenedetti, "Evolution from surface-influenced to bulk-like dynamics in nanoscopically confined water," J. Phys. Chem. B **113**, 7973–7976 (2009).
[11] D. E. Moilanen, E. E. Fenn, D. B. Wong, and M. D. Fayer, "Water dynamics in large and small reverse micelles: From two ensembles to collective behavior," J. Chem. Phys. **131**, 014704 (2009).
[12] E. E. Fenn, D. B. Wong, and M. D. Fayer, "Water dynamics at neutral and ionic interfaces," Proc. Nat. Acad. Sci. U. S. A. **106**, 15243 (2009).
[13] P. A. Pieniazek, Y.-S. Lin, J. Chowdhary, B. M. Ladanyi, and J. L. Skinner, "Vibrational spectroscopy and dynamics of water confined inside reverse micelles," J. Phys. Chem. B **113**, 15017–15028 (2009).
[14] P. K. Singh, D. G. Kuroda, and R. M. Hochstrasser, "An ion's perspective on the molecular motions of nanoconfined water: A two-dimensional infrared spectroscopy study," J. Phys. Chem. B **117**, 9775–9784 (2013).

[15]A. A. Bakulin, D. Cringus, P. A. Pieniazek, J. L. Skinner, T. L. C. Jansen, and M. S. Pshenichnikov, "Dynamics of water confined in reversed micelles: Multidimensional vibrational spectroscopy study," J. Phys. Chem. B **117**, 15545–15558 (2013).
[16]R. Yuan, C. Yan, J. Nishida, and M. D. Fayer, "Dynamics in a water interfacial boundary layer investigated with IR polarization selective pump-probe experiments," J. Phys. Chem. B **121**, 4530–4537 (2017).
[17]W. H. Thompson, "Perspective: Dynamics of confined liquids," J. Chem. Phys. **149**, 170901 (2018).
[18]S. A. Yamada, J. Y. Shin, W. H. Thompson, and M. D. Fayer, "Water dynamics in nanoporous silica: Ultrafast vibrational spectroscopy and molecular dynamics simulations," J. Phys. Chem. C **123**, 5790–5803 (2019).
[19]J. Y. Shin, S. A. Yamada, and M. D. Fayer, "Dynamics of a room temperature ionic liquid in supported ionic liquid membranes vs the bulk liquid: 2D IR and polarized IR pump–probe experiments," J. Am. Chem. Soc. **139**, 311–323 (2017).
[20]R. S. Anaredy and S. K. Shaw, "Long-range ordering of ionic liquid fluid films," Langmuir **32**, 5147–5154 (2016).
[21]J. Nishida, J. P. Breen, B. Wu, and M. D. Fayer, "Extraordinary slowing of structural dynamics in thin films of a room temperature ionic liquid," ACS Cent. Sci. **4**, 1065–1073 (2018).
[22]J. N. Israelachvili and R. M. Pashley, "Molecular layering of water at surfaces and origin of repulsive hydration forces," Nature **306**, 249–250 (1983).
[23]I. C. Bourg and C. I. Steefel, "Molecular dynamics simulations of water structure and diffusion in silica nanopores," J. Phys. Chem. C **116**, 11556–11564 (2012).
[24]D. E. Moilanen, I. R. Piletic, and M. D. Fayer, "Water dynamics in Nafion fuel cell membranes: The effects of confinement and structural changes on the hydrogen bond network," J. Phys. Chem. C **111**, 8884–8891 (2007).
[25]R. Musat, J. P. Renault, M. Candelaresi, D. J. Palmer, S. L. Caër, R. Righini, and S. Pommeret, "Finite size effects on hydrogen bonds in confined water," Angew. Chem., Int. Ed. **47**, 8033–8035 (2008).
[26]J. Chowdhary and B. M. Ladanyi, "Molecular dynamics simulation of aerosol-OT reverse micelles," J. Phys. Chem. B **113**, 15029–15039 (2009).
[27]A. A. Milischuk and B. M. Ladanyi, "Structure and dynamics of water confined in silica nanopores," J. Chem. Phys. **135**, 174709 (2011).
[28]D. Laage and W. H. Thompson, "Reorientation dynamics of nanoconfined water: Power-law decay, hydrogen-bond jumps, and test of a two-state model," J. Chem. Phys. **136**, 044513 (2012).
[29]A. A. Milischuk and B. M. Ladanyi, "Polarizability anisotropy relaxation in nanoconfinement: Molecular simulation study of water in cylindrical silica pores," J. Chem. Phys. **141**, 18C513 (2014).
[30]P. C. Burris, D. Laage, and W. H. Thompson, "Simulations of the infrared, Raman, and 2D-IR photon echo spectra of water in nanoscale silica pores," J. Chem. Phys. **144**, 194709 (2016).
[31]M. Heyden, "Heterogeneity of water structure and dynamics at the protein-water interface," J. Chem. Phys. **150**, 094701 (2019).
[32]C. J. Huber, S. M. Egger, I. C. Spector, A. R. Juelfs, C. L. Haynes, and A. M. Massari, "2D-IR spectroscopy of porous silica nanoparticles: Measuring the distance sensitivity of spectral diffusion," J. Phys. Chem. C **119**, 25135–25144 (2015).
[33]C. D. Norton and W. H. Thompson, "Reorientation dynamics of nanoconfined acetonitrile: A critical examination of two-state models," J. Phys. Chem. B **118**, 8227–8235 (2014).
[34]J. S. Beck, J. C. Vartuli, W. J. Roth, M. E. Leonowicz, C. T. Kresge, K. D. Schmitt, C. T. W. Chu, D. H. Olson, E. W. Sheppard, S. B. McCullen, J. B. Higgins, and J. L. Schlenker, "A new family of mesoporous molecular sieves prepared with liquid crystal templates," J. Am. Chem. Soc. **114**, 10834–10843 (1992).
[35]C. T. Kresge, M. E. Leonowicz, W. J. Roth, J. C. Vartuli, and J. S. Beck, "Ordered mesoporous molecular sieves synthesized by a liquid-crystal template mechanism," Nature **359**, 710 (1992).
[36]D. Zhao, J. Feng, Q. Huo, N. Melosh, G. H. Fredrickson, B. F. Chmelka, and G. D. Stucky, "Triblock copolymer syntheses of mesoporous silica with periodic 50 to 300 angstrom pores," Science **279**, 548–552 (1998).
[37]H. Bian, X. Wen, J. Li, and J. Zheng, "Mode-specific intermolecular vibrational energy transfer. II. Deuterated water and potassium selenocyanate mixture," J. Chem. Phys. **133**, 034505 (2010).
[38]S. Park, M. Ji, and K. J. Gaffney, "Ligand exchange dynamics in aqueous solution studied with 2D IR spectroscopy," J. Phys. Chem. B **114**, 6693–6702 (2010).
[39]Z. Sun, W. Zhang, M. Ji, R. Hartsock, and K. J. Gaffney, "Contact ion pair formation between hard acids and soft bases in aqueous solutions observed with 2DIR spectroscopy," J. Phys. Chem. B **117**, 15306–15312 (2013).
[40]H. Bian, H. Chen, Q. Zhang, J. Li, X. Wen, W. Zhuang, and J. Zheng, "Cation effects on rotational dynamics of anions and water molecules in alkali (Li^+, Na^+, K^+, Cs^+) thiocyanate (SCN^-) aqueous solutions," J. Phys. Chem. B **117**, 7972–7984 (2013).
[41]H. Bian, J. Li, Q. Zhang, H. Chen, W. Zhuang, Y. Q. Gao, and J. Zheng, "Ion segregation in aqueous solutions," J. Phys. Chem. B **116**, 14426–14432 (2012).
[42]D. Zhou, Q. Wei, S. Wang, X. Li, and H. Bian, "Counterion effect on vibrational relaxation and the rotational dynamics of interfacial water and an anionic vibrational probe in the confined reverse micelles environment," J. Phys. Chem. Lett. **10**, 176–182 (2019).
[43]S. A. Yamada, W. H. Thompson, and M. D. Fayer, "Water-anion hydrogen bonding dynamics: Ultrafast IR experiments and simulations," J. Chem. Phys. **146**, 234501 (2017).
[44]K. Kwak, S. Park, I. J. Finkelstein, and M. D. Fayer, "Frequency-frequency correlation functions and apodization in two-dimensional infrared vibrational echo spectroscopy: A new approach," J. Chem. Phys. **127**, 124503 (2007).
[45]K. Kwak, D. E. Rosenfeld, and M. D. Fayer, "Taking apart the two-dimensional infrared vibrational echo spectra: More information and elimination of distortions," J. Chem. Phys. **128**, 204505 (2008).
[46]P. Hamm and M. T. Zanni, *Concepts and Methods of 2D Infrared Spectroscopy* (Cambridge University Press, New York, 2011).
[47]R. Kubo, in *Fluctuation, Relaxation and Resonance in Magnetic Systems*, edited by D. T. Haar (Oliver and Boyd, London, 1961).
[48]A. Tokmakoff, "Orientational correlation functions and polarization selectivity for nonlinear spectroscopy of isotropic media. I. Third order," J. Chem. Phys. **105**, 1–12 (1996).
[49]H.-S. Tan, I. R. Piletic, and M. D. Fayer, "Polarization selective spectroscopy experiments: Methodology and pitfalls," J. Opt. Soc. Am. B **22**, 2009–2017 (2005).
[50]S. Li, T. D. Shepherd, and W. H. Thompson, "Simulations of the vibrational relaxation of a model diatomic molecule in a nanoconfined polar solvent," J. Phys. Chem. A **108**, 7347–7355 (2004).
[51]S.-H. Shim and M. T. Zanni, "How to turn your pump-probe instrument into a multidimensional spectrometer: 2D IR and vis spectroscopies via pulse shaping," Phys. Chem. Chem. Phys. **11**, 748–761 (2009).
[52]J. Nishida, A. Tamimi, H. Fei, S. Pullen, S. Ott, S. M. Cohen, and M. D. Fayer, "Structural dynamics inside a functionalized metal–organic framework probed by ultrafast 2D IR spectroscopy," Proc. Nat. Acad. Sci. U. S. A. **111**, 18442–18447 (2014).
[53]H. J. C. Berendsen, J. R. Grigera, and T. P. Straatsma, "The missing term in effective pair potentials," J. Phys. Chem. **91**, 6269–6271 (1987).
[54]J.-P. Ryckaert, G. Ciccotti, and H. J. C. Berendsen, "Numerical integration of the Cartesian equations of motion of a system with constraints: Molecular dynamics of N-alkanes," J. Comput. Phys. **23**, 327–341 (1977).
[55]T. S. Gulmen and W. H. Thompson, "Model silica pores with controllable surface chemistry for molecular dynamics simulations," MRS Online Proc. Libr. **899**, 0899-N6-N05 (2005).
[56]T. S. Gulmen and W. H. Thompson, "Testing a two-state model of nanoconfined liquids: Conformational equilibrium of ethylene glycol in amorphous silica pores," Langmuir **22**, 10919–10923 (2006).
[57]R. T. Cygan, J.-J. Liang, and A. G. Kalinichev, "Molecular models of hydroxide, oxyhydroxide, and clay phases and the development of a general force field," J. Phys. Chem. B **108**, 1255–1266 (2004).
[58]C. J. Fennell and J. D. Gezelter, "Is the Ewald summation still necessary? Pairwise alternatives to the accepted standard for long-range electrostatics," J. Chem. Phys. **124**, 234104 (2006).
[59]D. P. Shoemaker, C. W. Garland, and J. W. Nibler, *Experiments in Physical Chemistry* (McGraw-Hill, New York, 1989).
[60]R. Yuan, C. Yan, A. Tamimi, and M. D. Fayer, "Molecular anion hydrogen bonding dynamics in aqueous solution," J. Phys. Chem. B **119**, 13407–13415 (2015).

[61] V. Bolis, B. Fubini, L. Marchese, G. Martra, and D. Costa, "Hydrophilic and hydrophobic sites on dehydrated crystalline and amorphous silicas," J. Chem. Soc., Faraday Trans. **87**, 497–505 (1991).
[62] J. Chen, Q. Li, R. Xu, and F. Xiao, "Distinguishing the silanol groups in the mesoporous molecular sieve MCM-41," Angew. Chem., Int. Ed. Engl. **34**, 2694–2696 (1996).
[63] B. Grünberg, T. Emmler, E. Gedat, I. Shenderovich, G. H. Findenegg, H.-H. Limbach, and G. Buntkowsky, "Hydrogen bonding of water confined in mesoporous silica MCM-41 and SBA-15 studied by ^{1}H solid-state NMR," Chem.-Eur. J. **10**, 5689–5696 (2004).
[64] M. Gierada, I. Petit, J. Handzlik, and F. Tielens, "Hydration in silica based mesoporous materials: A DFT model," Phys. Chem. Chem. Phys. **18**, 32962–32972 (2016).
[65] X. F. Huang, Q. Wang, X. X. Liu, S. H. Yang, C. X. Li, G. Sun, L. Q. Pan, and K. Q. Lu, "Vibrational dynamics of water within mesoporous materials at different hydration levels during adsorption and desorption processes," J. Phys. Chem. C **113**, 18768–18771 (2009).
[66] D. E. Moilanen, I. R. Piletic, and M. D. Fayer, "Tracking water's response to structural changes in Nafion membranes," J. Phys. Chem. A **110**, 9084–9088 (2006).
[67] S. A. Roget, P. L. Kramer, J. E. Thomaz, and M. D. Fayer, "Bulk-like and interfacial water dynamics in Nafion fuel cell membranes investigated with ultrafast nonlinear IR spectroscopy," J. Phys. Chem. B **123**, 9408–9417 (2019).
[68] S. A. Corcelli and J. L. Skinner, "Infrared and Raman line shapes of dilute HOD in liquid H_2O and D_2O from 10 to 90 °C," J. Phys. Chem. A **109**, 6154–6165 (2005).
[69] G. Lipari and A. Szabo, "Effect of librational motion on fluorescence depolarization and nuclear magnetic resonance relaxation in macromolecules and membranes," Biophys. J. **30**, 489–506 (1980).
[70] P. Debye, *Polar Molecules* (Dover, New York, 1929).
[71] Y. L. A. Rezus and H. J. Bakker, "On the orientational relaxation of HDO in liquid water," J. Chem. Phys. **123**, 114502 (2005).
[72] S. Park and M. D. Fayer, "Hydrogen bond dynamics in aqueous NaBr solutions," Proc. Nat. Acad. Sci. U. S. A. **104**, 16731–16738 (2007).
[73] D. Laage and J. T. Hynes, "On the molecular mechanism of water reorientation," J. Phys. Chem. B **112**, 14230–14242 (2008).
[74] R. Kumar, J. R. Schmidt, and J. L. Skinner, "Hydrogen bonding definitions and dynamics in liquid water," J. Chem. Phys. **126**, 204107 (2007).
[75] C. J. Fecko, J. D. Eaves, J. J. Loparo, A. Tokmakoff, and P. L. Geissler, "Ultrafast hydrogen-bond dynamics in the infrared spectroscopy of water," Science **301**, 1698–1702 (2003).
[76] C. J. Fecko, J. J. Loparo, S. T. Roberts, and A. Tokmakoff, "Local hydrogen bonding dynamics and collective reorganization in water: Ultrafast infrared spectroscopy of HOD/D_2O," J. Chem. Phys. **122**, 054506 (2005).
[77] J. B. Asbury, T. Steinel, C. Stromberg, S. A. Corcelli, C. P. Lawrence, J. L. Skinner, and M. D. Fayer, "Water dynamics: Vibrational echo correlation spectroscopy and comparison to molecular dynamics simulations," J. Phys. Chem. A **108**, 1107–1119 (2004).
[78] J. B. Asbury, T. Steinel, K. Kwak, S. A. Corcelli, C. P. Lawrence, J. L. Skinner, and M. D. Fayer, "Dynamics of water probed with vibrational echo correlation spectroscopy," J. Chem. Phys. **121**, 12431–12446 (2004).
[79] S. Park, K. Kwak, and M. D. Fayer, "Ultrafast 2D-IR vibrational echo spectroscopy: A probe of molecular dynamics," Laser Phys. Lett. **4**, 704 (2007).
[80] J. R. Schmidt, S. A. Corcelli, and J. L. Skinner, "Pronounced non-Condon effects in the ultrafast infrared spectroscopy of water," J. Chem. Phys. **123**, 044513 (2005).
[81] J. R. Reimers and L. E. Hall, "The solvation of acetonitrile," J. Am. Chem. Soc. **121**, 3730–3744 (1999).
[82] C. M. Morales and W. H. Thompson, "Simulations of infrared spectra of nanoconfined liquids: Acetonitrile confined in nanoscale, hydrophilic silica pores," J. Phys. Chem. A **113**, 1922–1933 (2009).
[83] A. C. Fogarty, E. Duboué-Dijon, D. Laage, and W. H. Thompson, "Origins of the non-exponential reorientation dynamics of nanoconfined water," J. Chem. Phys. **141**, 18C523 (2014).
[84] This is an approximation, given the definition of d as the distance from the $SeCN^{-}C$ atom to the nearest pore O atom. This distance is not always measured precisely in the radial direction.
[85] J. Faeder and B. M. Ladanyi, "Solvation dynamics in reverse micelles: The role of headgroup—solute interactions," J. Phys. Chem. B **109**, 6732–6740 (2005).